remote sensing

MDPI

Article

UAV-Based Photogrammetric Inspection in Deep Vertical Shafts: A Case Study from the KGHM GG-1 Mineshaft in Poland

Wojciech Rutkowski [1,2,*], Jędrzej Szczepaniak [3], Tomasz Lipecki [1] and Antoni Rzonca [1]

[1] The Faculty of Geo-Data Science, Geodesy, and Environmental Engineering, AGH University of Krakow, 30-059 Kraków, Poland; tomasz.lipecki@agh.edu.pl (T.L.); antoni.rzonca@agh.edu.pl (A.R.)
[2] Przedsiębiorstwo Budowy Kopalń PeBeKa S.A. KGHM Group, Marii Skłodowskiej-Curie 76, 59-300 Lubin, Poland
[3] The Faculty of Electronics, Photonics and Microsystems, Wrocław University of Science and Technology, 50-370 Wrocław, Poland; jedrzej.szczepaniak@pwr.edu.pl
* Correspondence: wrutkows@agh.edu.pl or wojciech.rutkowski@agh.edu.pl

Highlights

What are the main findings?

- A custom UAV-based photogrammetric system was developed for GNSS-denied deep mineshaft inspection.
- UAV-based image acquisition enabled 3D visual documentation of shaft lining and infrastructure in a confined underground environment.

What is the implication of the main finding?

- The proposed approach can support conventional shaft inspections by improving remote visual documentation while reducing the need for direct personnel exposure.
- The obtained accuracy is more suitable for inspection-oriented documentation and hazard identification than for millimeter-level geodetic monitoring.

Abstract

Underground mining operations depend heavily on vertical shafts for access, ventilation, and ore transport, making their structural integrity and safety critical to overall mine performance. Traditional shaft inspections, though rigorous, are limited by human accessibility, environmental hazards, and subjective evaluation. This study presents the development and initial testing of a novel unmanned aerial vehicle (UAV) system designed specifically for shaft inspections in deep mining environments. The research focuses on the GG-1 shaft in Kwielice, Poland—the country's deepest operational shaft—where challenging conditions such as high ventilation airflow, confined geometry, and absence of GNSS signals necessitated innovative solutions. A custom-built hexacopter equipped with high-resolution cameras and photogrammetric capabilities was deployed to capture detailed visual and spatial data. This article presents complementary path of UAV evolution, from concept, early development stage and results without positioning system through to the description of final results including positioning system and all six cameras until results of high-altitude flights. Results demonstrate that UAV-based inspection can deliver sufficient precision for identifying structural irregularities, documenting shaft infrastructure, and enhancing safety monitoring. The findings highlight the potential of UAV technology as a complementary tool to conventional inspections, offering improved data quality, reduced risk to personnel, and a new approach to shaft maintenance.

Keywords: UAV; photogrammetry; mining; remote sensing; mineshaft; shaft sinking

Check for updates

Academic Editors: Hanyun Wang, Li Li, Qi Dong and Yao Wei

Received: 16 May 2026
Revised: 26 June 2026
Accepted: 2 July 2026
Published: 7 July 2026

Copyright: © 2026 by the authors. Licensee MDPI, Basel, Switzerland. This article is an open access article distributed under the terms and conditions of the Creative Commons Attribution (CC BY) license.

1. Introduction

The majority of underground mining operations rely on vertical mineshafts as their primary means of access, ventilation, and material transport. As ore bodies are increasingly located at greater depths and in more geologically complex settings, vertical shafts offer superior efficiency from both technical and economic standpoints compared to inclined entries. Their design and construction allow for high-capacity hoisting systems and minimized haulage distances, which are critical in modern deep mining scenarios. However, the operation of a mineshaft involves continuous exposure to a range of challenging environmental and geological factors. These include high rock mass pressure, hydrostatic pressure from groundwater, and seasonal fluctuations in temperature and humidity [1–3]. Such conditions place considerable stress on the shaft infrastructure, including cable routes, hoisting guides, rail guides, and utility lines. This infrastructure is subject to both internal deterioration and external environmental influences, resulting in a need for consistent monitoring and maintenance. In addition to infrastructure degradation, the shaft lining—commonly composed of concrete or cast-iron tubbing—is also susceptible to long-term damage [4–6]. Concrete linings may undergo chemical degradation or physical cracking due to stress concentration, while cast-iron tubbing can fracture or experience bolt shear under sustained water pressure or seismic events. Over time, these issues can compromise the structural integrity of the shaft and present significant operational and safety risks. Given the critical role of the mineshaft in the overall mining system, its maintenance is of fundamental importance. A well-maintained shaft ensures safe access for personnel, uninterrupted transport of materials, and reliable operation of essential services. To maintain shaft integrity and functionality, a comprehensive maintenance strategy is required—one that includes routine inspections, preventive repairs, and emergency interventions when necessary. Among these strategies, systematic shaft inspections are a cornerstone of proactive maintenance. In accordance with Polish Geological and Mining Law [7], and relevant ministerial regulations [8], inspections are mandated at regular intervals that vary depending on shaft conditions and operational status. These intervals may be daily, weekly, monthly, or quarterly. For shafts undergoing construction, deepening, or extensive repair activities, daily inspections are obligatory and must be performed at the beginning of each working shift. In the Polish underground mining industry, daily shaft inspections are conducted by certified professionals who possess specialized training in shaft operations and safety. These inspections involve a range of diagnostic activities, including visual evaluation of the shaft lining and infrastructure, mechanical testing of bolted connections, identification of water inflows and leaks, detection of structural deformation, and assessment of hoisting system components. Overall, rigorous inspection protocols play a vital role in ensuring the long-term safety and operational reliability of underground mineshafts. They enable early detection of deterioration, facilitate timely intervention, and contribute to the sustainable development of deep mining operations. While inspection personnel are typically well-trained and protocols are carefully developed, it is important to recognize that inspections are ultimately conducted by human operators. As such, factors such as fatigue, limited accessibility, and variable environmental conditions can influence the consistency and scope of inspection activities. The authors suggest that supplementing daily shaft inspections with robotic systems, such as unmanned aerial vehicles (UAVs), may provide additional benefits, particularly in enhancing coverage and improving data collection. The use of robotic and UAV-based inspection systems is becoming increasingly common in the mining industry [9–11]. At the same time, recent advances in GNSS-denied navigation and underground mapping have improved the practical applicability of such systems in confined and subterranean environments [12–14]. UAVs can assist in reaching areas that are difficult or unsafe for personnel to access and can capture high-resolution

visual data efficiently. When equipped with appropriate sensors, UAVs can support early detection of structural issues and help standardize inspection processes. Incorporating robotic systems into routine inspection workflows may not replace human expertise but can serve as a valuable complement, contributing to improved safety, documentation, and maintenance planning in shaft operations.

1.1. Research Object—GG-1 Mineshaft in Kwielice, Poland

The GG-1 mineshaft, located in Kwielice in southwestern Poland, is the newest and currently the deepest operational mineshaft in the country. Shaft sinking process was finished in December 2022 by Przedsiębiorstwo Budowy Kopalń PeBeKa S.A. which is KGHM's main contractor for shaft sinking projects. Similar to other mineshafts operated by KGHM Polska Miedź S.A., GG-1 is situated within the Fore-Sudetic Monocline, in the Lower Silesian Voivodeship. This geological region forms part of the Legnica-Głogów Copper District (LGCD), a major center of copper ore mining in Poland. The general location of the LGOM area is shown in Figure 1.

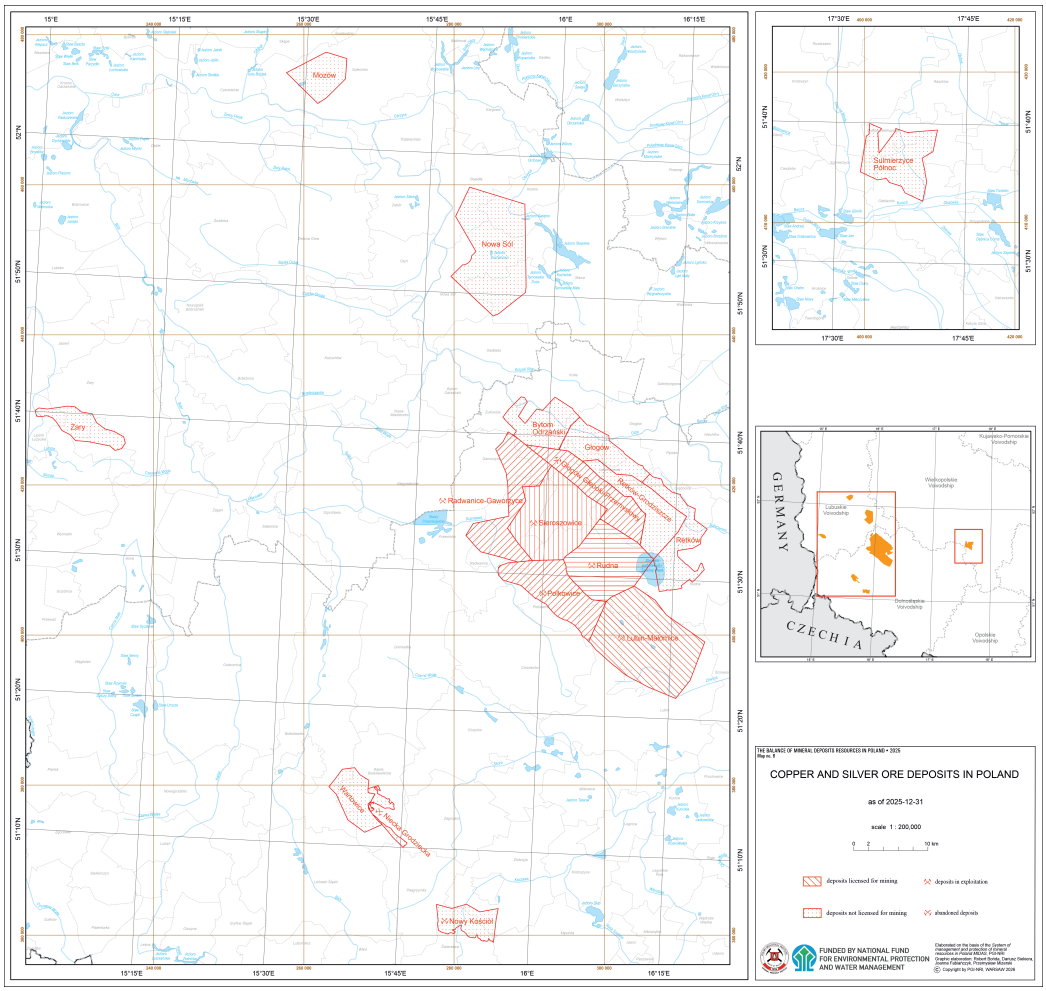

Figure 1. Mineral resources of Poland with highlighted Legnicko-Głogowski copper district [15].

The GG-1 mineshaft is part of the KGHM Polska Miedź S.A. Rudna mine and reaches a depth of 1351 m below ground level. At present, the shaft functions primarily as a ventilation intake; however, it is currently being equipped with rail guides to accommodate a hoisting cage in the future. Despite its distinction as the deepest shaft in Poland, the GG-1 mineshaft generally follows standard construction practices used by KGHM. The upper sections of the shaft, located within the freezing zone, are lined with cast-iron tubbing

to ensure watertight integrity in areas of high groundwater pressure. Below this zone, where less intensive sealing is required, the shaft is primarily lined with reinforced concrete. A distinguishing feature of GG-1 is the presence of two additional cast-iron tubbing columns at greater depths. The second tubbing column, consisting of 30 rings, was installed in response to significant water inflow encountered in dolomitic rock layers. A third column, comprising 52 double tubbing rings, was constructed within the rock salt interval to ensure structural stability against rock salt rheological properties. The ongoing shaft development works, conducted by Przedsiębiorstwo Budowy Kopalń PeBeKa S.A.—KGHM's primary contractor for shaft sinking—offer a valuable opportunity for the authors to design and test an unmanned aerial vehicle (UAV) system for use in shaft inspection and monitoring applications. A detailed overview of the design, development, and testing process of the proposed system, along with preliminary results and observations, will be presented in the following sections.

1.2. Mineshaft Inspections Methods

According to Polish regulations, mine shafts during the sinking process are required to undergo daily inspections performed by certified inspectors. This practice is well established, having been applied worldwide for several decades. In the case of operational mine shafts, where inspections are typically performed on a weekly basis, similar challenges persist due to the high costs associated with production downtime. Increasing costs related to ore hoisting and the overall operation of mine shafts compel mining companies to seek solutions for optimizing inspection time and procedures. The rapid development of unmanned technologies enables mining companies to incorporate autonomous or semi-autonomous systems to enhance inspection procedures and, in the long term, to reduce the frequency of inspections performed by personnel. Project Lazarus, developed by Canadian company POINT.LAZ [16], is a representative example of this innovative approach. The compact device is clamped to the mine shaft conveyance cable and hoisted along the shaft. According to the manufacturer, a hybrid measurement method combining spherical imaging data and laser scanning enables the generation of a complete three-dimensional shaft model with a global accuracy better than 15 mm and, using a dedicated system for guide inspection, a local detail accuracy better than 5 mm [16]. This system represents the current state of the art in shaft inspection technologies, an approach that has also been investigated and implemented by various manufacturers and research institutions. Comparable measurement services are offered, among others, by the German company DMT Group [17] and the Polish company Scala 3D [18]. An in-depth comparison of inspection and measurement methods used in mine shaft sinking has been presented in a previous study by one of the authors [19].

2. Materials and Methods

This section describes the design process of an unmanned aerial vehicle (UAV) developed for underground flights. It presents the camera selection and design of the photogrammetric module, followed by a description of the underground experiments conducted during the development and validation of the platform.

2.1. Evolution of UAV Design

The concept of enhancing mineshaft inspections with unmanned aerial vehicles (UAVs) emerged from the authors' direct observations of current inspection practices. Despite the high level of expertise and experience of inspection personnel, conventional visual assessments remain inherently limited by human perception and may be affected by fatigue, interpretation variability, and difficult environmental conditions. Therefore, the authors

identified an opportunity to improve inspection reliability and safety through the application of robotics and automation. Importantly, the proposed solution was not intended to replace inspection personnel, but rather to provide additional, objective documentation that could be analyzed by a broader group of specialists and support the identification of potential hazards.

This observation initiated a discussion on the feasibility of developing a UAV system capable of operating safely and effectively in the challenging environment of a vertical mineshaft. Several factors complicate UAV operation in such conditions, including the presence of large steel structures, fluctuating air pressure, forced ventilation currents, high humidity or rainfall, poor visibility, confined space, and the absence of Global Navigation Satellite System (GNSS) signals for positioning. These constraints create significant technical barriers, particularly for maintaining stable flight within a limited horizontal space. Although the diameter of the mineshaft is 7.5 m for GG-1, the effective available space was only 4.5 m.

Instead of introducing an entirely new reference infrastructure, the authors decided to use an element already required by Polish mining regulations [8] in shafts under construction: the central steel alignment line. This 6 mm diameter steel line, used during shaft sinking as a vertical reference for structural alignment, was identified as a potential resource for UAV stabilization, positioning, and operational safety.

Based on this idea, the UAV design concept was developed to use the steel line as a passive guidance and positioning aid. Although the first concept was relatively simple, it established the fundamental design direction for further development. A preliminary 3D model of this initial design is presented in Figure 2.

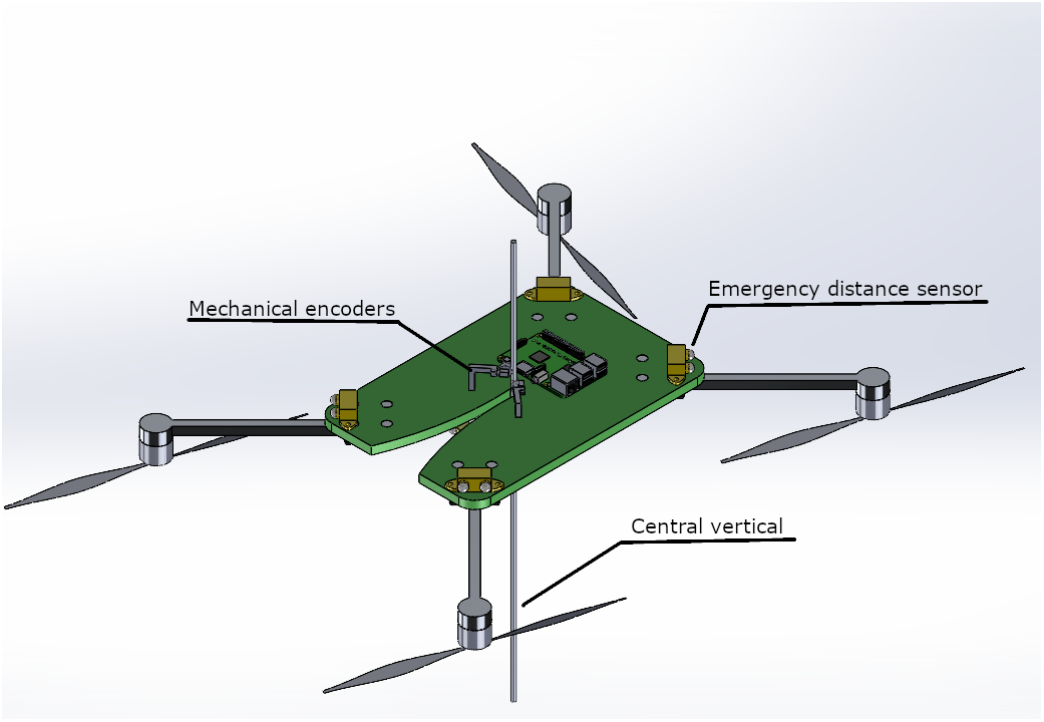

Figure 2. First conceptual 3D model of the UAV for mineshaft inspection.

As previously mentioned, the central steel alignment line was initially intended to serve both as a stabilization aid and as a reference element for positioning. One of the first proposed solutions for determining vertical displacement was a depth odometry system based on mechanical encoders. This approach could have allowed the UAV to remain

centered within the shaft while simultaneously providing continuous information on its vertical position.

However, this concept was ultimately abandoned. The main limitation was the conflict between the mechanical constraints introduced by the encoder-based system and the UAV flight control algorithms, which are designed for unconstrained six-degree-of-freedom motion. Directly constraining the UAV to a physical guide introduced undesirable interactions with the control system and increased the risk of instability. For this reason, the fully mechanical approach was considered unsuitable for practical implementation.

Although the fully mechanical concept was abandoned, the idea of using the central steel alignment line both as a positional reference and as an operational constraint remained unchanged. Details of the sensor setup was describe in Section 2.2.

The final UAV platform evolved into a hexacopter with a motor-to-motor span of 1.2 m and a total span of approximately 1.7 m measured between the propeller tips. The maximum take-off mass of the platform is 25 kg, while the mass of the UAV in flight-ready configuration, without the photogrammetric module, is approximately 10.5 kg. The photogrammetric module described in the following section has a mass of approximately 5 kg and consists of six high-resolution cameras arranged to provide circumferential image acquisition. The first underground flights were performed with a simplified three-camera configuration, while the final version of the system used the complete six-camera photogrammetric module. The 3D model of the final UAV design is presented in Figure 3 below.

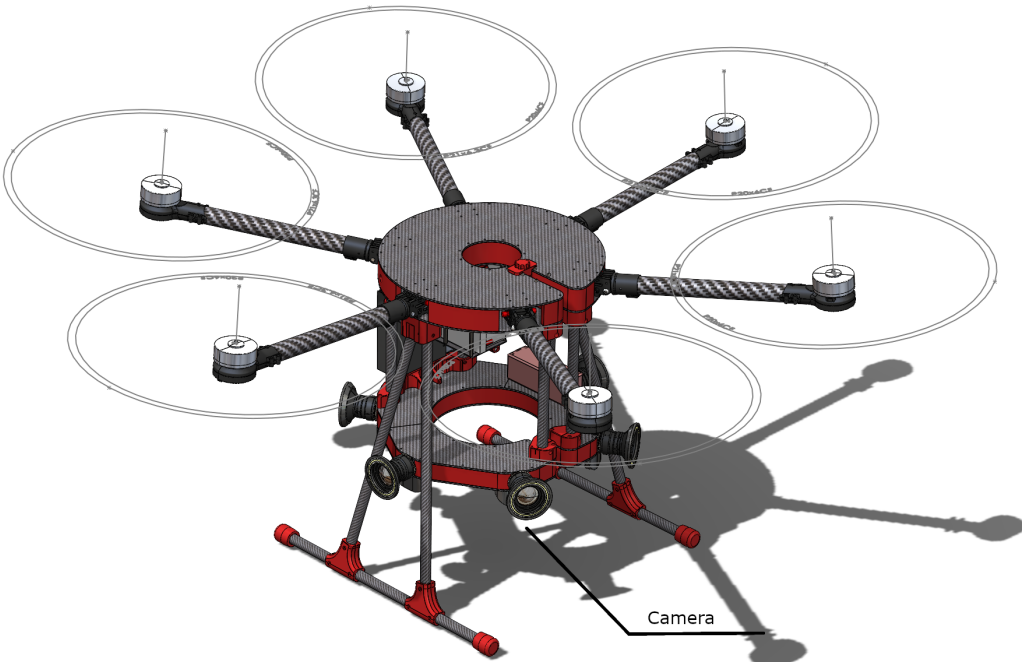

Figure 3. Latest model of UAV for mineshaft inspection with installed camera module.

Figure 4 presents photographs from the first underground trials of the UAV without the final photogrammetric module.

The initial underground trial was conducted to verify the basic capability of the UAV to operate in underground shaft conditions and to collect sensor data required for the development of the positioning system. During this phase, a series of test flights was performed, each reaching a maximum vertical distance of approximately 10 m. Although this distance represented only a small fraction of the total shaft depth, the limitation was introduced deliberately as a safety measure, since the dedicated positioning algorithms were still under development at that stage.

Despite these constraints, the trial successfully demonstrated the UAV's ability to maintain stable flight within the confined space of the shaft, which was lined with cast-iron tubbing. In addition to vertical flight tests, the horizontal displacement capability of the UAV was evaluated through controlled dynamic maneuvers intended to laterally displace the central steel alignment line. This allowed the authors to assess the maximum deviation of the UAV from the shaft center under controlled conditions.

The maximum observed horizontal displacement did not exceed 15 cm. This result was considered highly satisfactory, particularly because the closest potential obstacle to the UAV propellers was located more than 2 m from the shaft center. Consequently, even under the observed horizontal displacement, more than 1 m of clearance to the nearest shaft infrastructure was maintained.

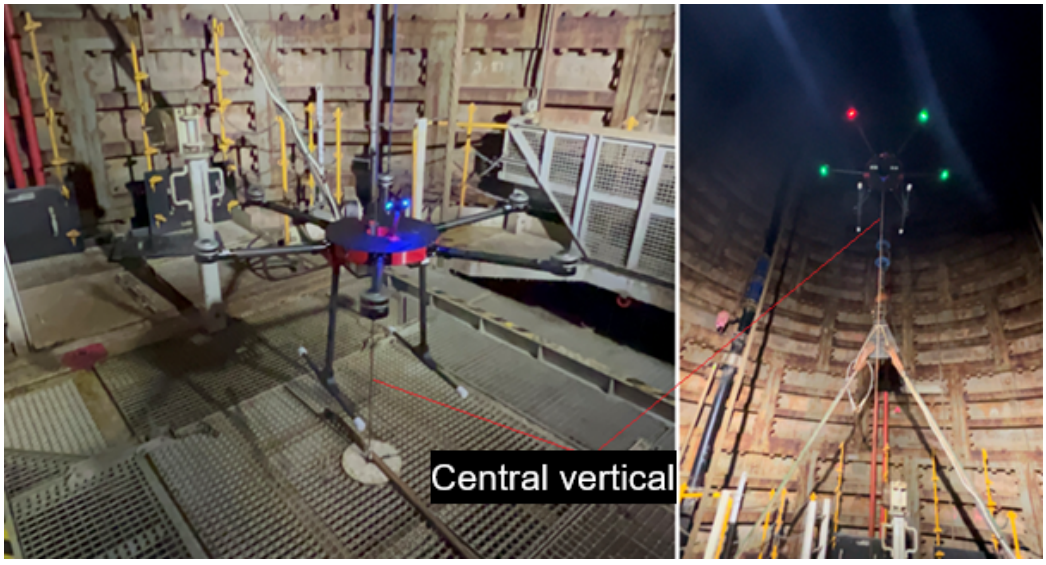

Figure 4. Photographs from the first underground trial of the UAV for mineshaft inspections (without photogrammetric module).

2.2. Central Vertical-Based UAV Positioning System

In the final configuration, the UAV was equipped with a dedicated positioning and navigation module consisting of additional sensors: two VL53L4CD Time-of-Flight (ToF) manufactured by STMicroelectronics, Geneve, Switzerland and one PAT9136KS manufactured by PixArt Imaging Inc., Hsinchu, Taiwan optical motion sensor. The two ToF displacement sensors were used to support horizontal positioning and to keep the UAV as close as possible to the center of the mineshaft. One of these sensors measured the distance to the central vertical along the UAV body-frame X axis, while the other measured the distance along the Y axis. The optical motion sensor was used to estimate vertical displacement from visual changes observed on the surface of the steel line. A 3D mechanical model of the positioning and navigation module is presented in Figure 5. The system data flow is shown on the diagram presented in Figure 6.

Data from these additional sensors were processed by a dedicated odometry algorithm developed specifically for this application and then integrated with the standard PX4 [20] state estimation framework in firmware version 1.15.4. Therefore, the shaft-relative positioning system relies on two primary measurement sources. The horizontal displacement from the central guide is determined by two VL53L4CD Time-of-Flight (ToF) distance sensors. These VL53L4CD sensors run at a 50 Hz refresh rate, providing a distance measurement accuracy of ± 2 mm. They are positioned along two perpendicular body-frame axes of the UAV on the linear guides of the trolley assembly, as illustrated in Figure 5. Retroreflective tape is placed in front of the ToF sensors to ensure low-noise, precise measurements across

the entire range of motion, even under harsh environmental conditions. The linear guide ensures smooth planar movement for the trolley, which holds a sensor for vertical observations. The trolley permits free angular variation in the pitch axis of the drone, while its roll movement is mechanically restricted to approximately ±15 deg.

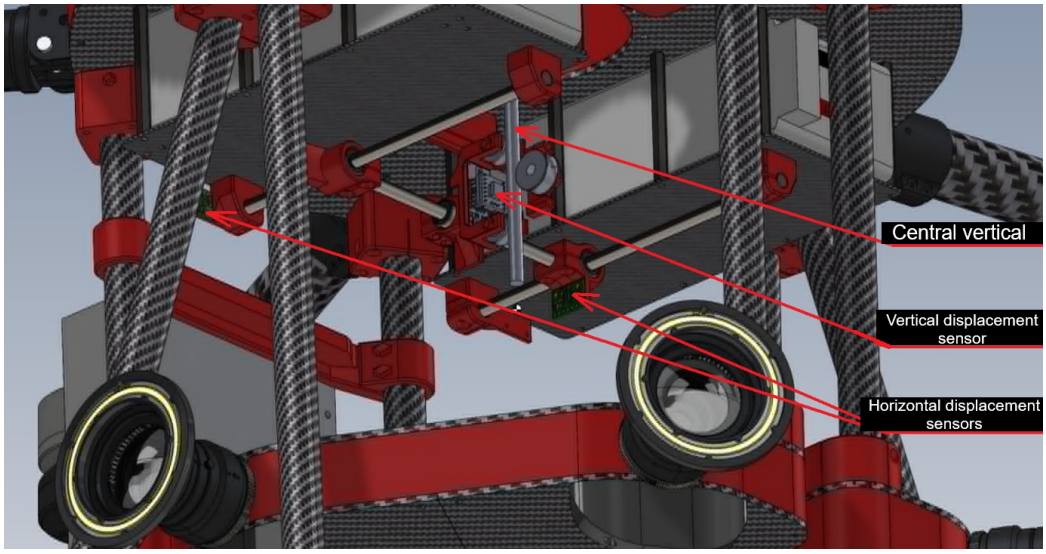

Figure 5. 3D model of the UAV positioning and navigation module based on the central steel alignment line.

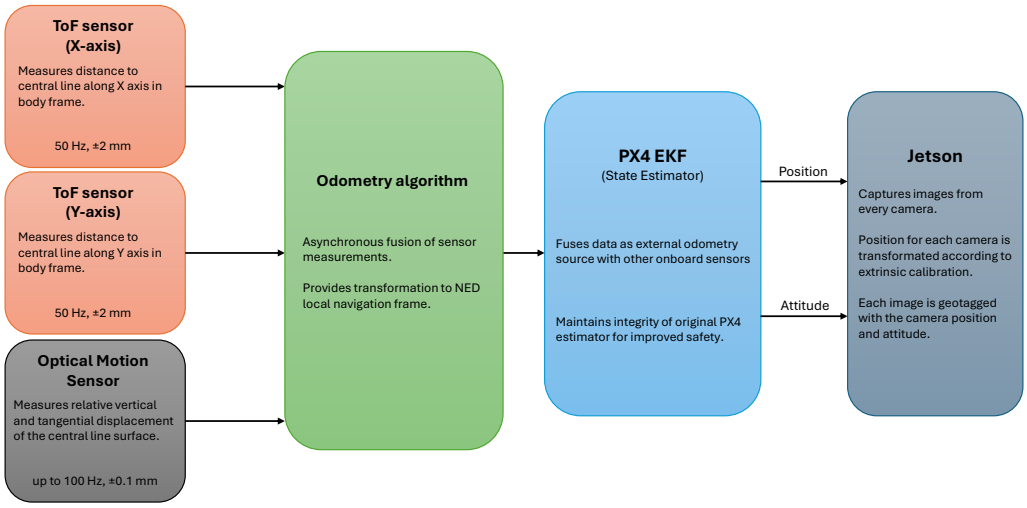

Figure 6. Data flow chart of the central vertical positioning system for stabilization and image geotagging.

Vertical tracking is performed by a PixArt PAT9136KS optical motion sensor equipped with a custom carrier board, mounted directly onto the trolley (Figure 5). The PixArt PAT9136KS sensor captures displacement with submillimeter resolution, offering a relative accuracy of ±0.1 mm and delivering data reports at a sampling frequency of up to 100 Hz. The accumulated sensor counts are transformed into metric displacement based on the predefined sensor resolution. In this setup, one axis of the sensor is aligned with the vertical direction, while the orthogonal axis captures the tangential motion around the guide line. The vertical readings provide a direct measurement of relative displacement along the shaft axis, whereas the tangential data is utilized to estimate the relative yaw around the central guide.

The odometry algorithm calculates the relative translational displacement of the UAV relative to the central vertical reference line. Observations from each sensor are treated as separate scalar measurements. This approach permits asynchronous fusion of data from

different sensors, eliminating the need for uniform sampling rates and synchronization. The estimated UAV position and velocity relative to the guideline are transformed (translated and rotated) into a coordinate frame compatible with the external visual odometry system. The EKF implementation within the PX4 software supports external visual odometry as a substitute for GNSS data. This external odometry frame delivers position, velocity, and optional quaternion updates, which are fed into the PX4 estimation pipeline as an auxiliary data source. This modular design maintains the integrity of the original estimator and enhances flight safety by preventing direct modifications to the core PX4 EKF.

A detailed description of sensor configuration, positioning principles, and data-processing algorithms will be provided in a companion publication.

2.3. Photogrammetric Module and Camera Calibration

The photogrammetric system for UAV was equipped with six high-resolution Basler ace 2 cameras manufactured by Basler AG, Ahrensburg, Germany, each equipped with a 1″ GMAX 2518 sensor. The cameras feature a global shutter, a maximum frame rate of 20 fps, a resolution of 18.6 MP, and a pixel size of 2.5 × 2.5 µm. Their compact dimensions and low mass of only 85 g, made them suitable for UAV-based photogrammetric applications, where payload weight is a critical design constraint. Although the cameras are rated at a relatively low protection class, the risk of water penetration was limited by enclosing them inside the photogrammetric module housing.

Each camera was equipped with a Kowa LM8HC manufactured by Kowa Optimed Deutschland GmbH, Duesseldorf, Germany low-distortion C-mount lens designed for 1″ sensors. The lens provides an 8 mm focal length and an adjustable aperture range from F1.4 to F16. The relatively high aperture was particularly important for the proposed application, as the camera and lens selection was aimed at obtaining the shortest possible exposure time while maintaining sufficient image quality. This was necessary to reduce motion blur during image acquisition in underground flight conditions. Each camera is also equipped with an individual COB LED ring used as an illumination source during exposure. As a result, the imaging system did not rely on external lighting and each camera could operate under repeatable illumination conditions. All cameras were triggered by a synchronization signal from the autopilot, which ensured temporal consistency of the acquired images and their corresponding metadata.

All six cameras in the photogrammetric module were arranged uniformly around the UAV geometric center on a circular layout with a radius of 0.18325 m, measured to the camera sensor plane. The first camera was oriented with a yaw angle of 30° relative to the Front-Right-Down (FRD) body frame of the UAV, and each subsequent camera was rotated by 60° with respect to the previous one, providing full circumferential coverage. All cameras were mounted with a vertical offset of 0.1751 m relative to the UAV center of gravity (CoG). A 3D model of the final UAV design, including the complete six-camera photogrammetric module, is presented in Figure 3.

During the tests, an exposure time of 15 ms, combined with the relatively large sensor with global shutter, bright lens, and flash source, provided images with no noticeable motion blur at UAV speeds of up to 2 m/s. In addition, the UAV structure was designed with sufficient vertical separation between the main UAV module and the photogrammetric module to ensure that the motors and propellers remained outside the cameras' field of view.

The extrinsic parameters of the camera rig were first defined according to the design assumptions and the 3D model of the photogrammetric module. These expected parameters, expressed in the UAV body frame using the FRD convention, are presented in Table 1.

In this frame, the *X* axis points forward, the *Y* axis points to the right, and the *Z* axis points downward.

Table 1. Expected extrinsic parameters of the UAV camera rig according to the design assumptions, expressed in the FRD body frame.

Camera	*X* [m]	*Y* [m]	*Z* [m]	Yaw [°]	Pitch [°]	Roll [°]
Cam1	0.15870	0.09162	0.17510	30.0	0.0	0.0
Cam2	0.00000	0.18325	0.17510	90.0	0.0	0.0
Cam3	−0.15870	0.09162	0.17510	150.0	0.0	0.0
Cam4	−0.15870	−0.09162	0.17510	210.0	0.0	0.0
Cam5	0.00000	−0.18325	0.17510	270.0	0.0	0.0
Cam6	0.15870	−0.09162	0.17510	330.0	0.0	0.0

After the cameras had been installed in the photogrammetric module, the real extrinsic parameters were determined experimentally. The measurements were performed in the photogrammetry laboratory at the University of Agriculture in Kraków. Forty reference points were placed around the UAV at different heights and distances and were measured using a high-grade terrestrial laser scanner, the ScanStation P50 manufactured by Leica Camera AG, Wetzlar, Germany. The UAV was then positioned at the same location previously occupied by the scanner and acquired 14 image sessions at different yaw angles to cover a full 360° rotation. This procedure enabled the estimation of the actual relative positions and orientations of all cameras in the rig. The resulting extrinsic parameters are presented in Table 2. The scanned area and the estimated camera orientations are shown in Figure 7.

Table 2. Extrinsic parameters of the UAV camera rig estimated in Agisoft Metashape, expressed in the FRD body frame.

Camera	*X* [m]	*Y* [m]	*Z* [m]	Yaw [°]	Pitch [°]	Roll [°]
Cam1	0.15888	0.09151	0.17532	29.50241	0.16220	0.40646
Cam2	−0.00031	0.18352	0.17487	89.74083	0.00559	0.24219
Cam3	−0.15852	0.09167	0.17524	149.88119	−0.25985	0.73856
Cam4	−0.15886	−0.09150	0.17491	210.22299	−0.59983	−0.24154
Cam5	0.00034	−0.18303	0.17536	270.10449	−0.37296	−0.51835
Cam6	0.15855	−0.09170	0.17484	329.54809	0.07405	−0.65673

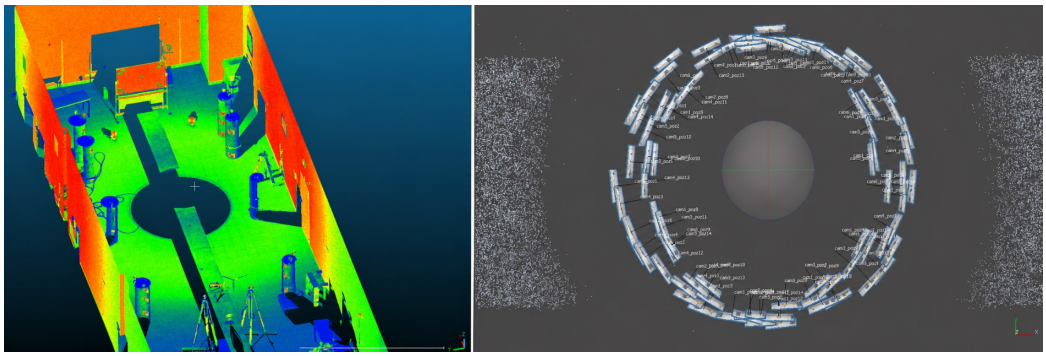

Figure 7. Part of scanned area (**left**); estimated camera orientation (**right**).

The comparison between the designed and estimated extrinsic parameters confirmed that the camera rig was assembled consistently with the assumptions adopted in the 3D model. Small deviations in camera position and angular orientation were expected due to manufacturing tolerances, mounting accuracy, and the mechanical assembly process.

The experimentally determined parameters were therefore used in further photogrammetric processing, as they better represented the real geometry of the camera rig than the nominal design values.

The intrinsic camera parameters were determined separately at AGH University of Krakow using a calibration wall equipped with Agisoft Metashape-compatible markers. The UAV during the intrinsic calibration procedure is shown in Figure 8. Each marker visible on the calibration wall was measured, which allowed the intrinsic parameters of all six cameras to be estimated in a repeatable and largely automated manner. The resulting parameters are presented in Table 3.

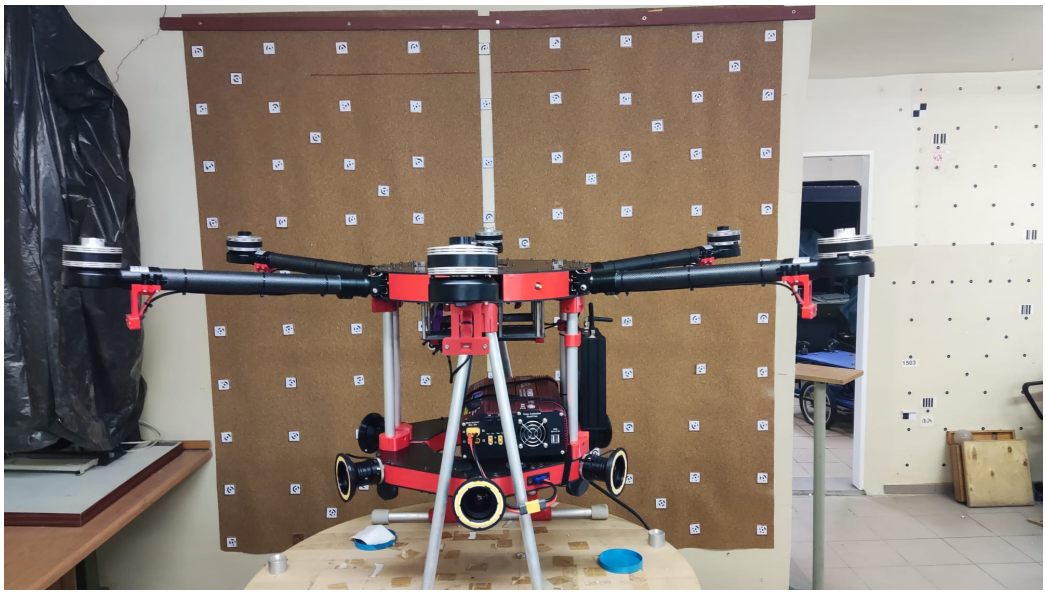

Figure 8. UAV during intrinsic parameters calibration at AGH University of Krakow.

Table 3. Intrinsic calibration parameters of the UAV cameras.

Parameter	Cam1	Cam2	Cam3	Cam4	Cam5	Cam6
Pixel size [µm]	2.5 × 2.5	2.5 × 2.5	2.5 × 2.5	2.5 × 2.5	2.5 × 2.5	2.5 × 2.5
Projection	fisheye	fisheye	fisheye	fisheye	fisheye	fisheye
Width [px]	4504	4504	4504	4504	4504	4504
Height [px]	4096	4096	4096	4096	4096	4096
f [px]	3317.18142	3302.58862	3304.90821	3311.92402	3311.64657	3303.26823
c_x [px]	13.0114	−49.2097	27.2172	13.6780	13.4090	−27.1622
c_y [px]	11.7056	−53.6985	−66.5242	−78.1338	−59.2941	−23.1383
k_1	−0.165433	−0.157386	−0.161834	−0.166138	−0.166985	−0.157821
k_2	0.103865	0.0847046	0.0983342	0.102875	0.107625	0.0849118
k_3	−0.0139425	0.0	−0.0110171	−0.0124911	−0.0168925	0.0
p_1	−0.000223139	−0.0000560575	−0.0000529813	−0.000479940	−0.000611337	−0.000199649
p_2	−0.000356764	0.0000846073	−0.000225719	−0.000127025	−0.0000755532	−0.000152889

The calibration parameters describe the internal geometry of each camera-lens unit. The image width and height define the sensor resolution in pixels. The parameter f denotes the focal length expressed in pixel units and represents the focal scaling used in photogrammetric projection. The parameters c_x and c_y describe the displacement of the principal point from the image center in the horizontal and vertical directions, respectively. The coefficients k_1, k_2, and k_3 represent radial lens distortion, while p_1 and p_2 describe tangential distortion caused mainly by small lens decentering or misalignment between

the lens and the sensor. For cameras where k_3 is not reported in the calibration file, this coefficient was not estimated in the adopted calibration model.

Although all cameras and lenses were of the same type, the calibration results show small differences between individual units. This is expected, as each lens–sensor pair is affected by manufacturing tolerances, small differences in lens centering, sensor placement, and assembly accuracy. These deviations are visible in the effective focal length, principal point location, and distortion coefficients. Therefore, using a single shared calibration for all cameras would introduce residual reprojection errors and could negatively affect image alignment, point cloud reconstruction, and metric accuracy [21,22]. For this reason, both intrinsic and extrinsic parameters were determined separately for each camera and used in the photogrammetric processing workflow.

Finally, the photogrammetric module was developed as an independent measurement unit and is not involved in the UAV navigation process. Its connection to the UAV is limited to a single Ethernet cable and camera trigger signal source, which simplifies integration and allows the module to be treated as a replaceable payload. This modular architecture facilitates camera recalibration when required and provides the possibility of replacing the photogrammetric module with another measurement system, such as a mobile laser scanner, in future developments.

2.4. Photogrammetric Fundamentals

The utilization of photogrammetry for documenting the internal surface of the shaft is enabled by efficient and automated methods for image-network alignment. In the presented case, the reconstruction is based on the structure-from-motion approach [23–25]. This method involves the automatic detection and matching of image features, followed by the estimation of camera exterior orientation parameters and object point coordinates through the solution of linearized collinearity equations using least-squares adjustment.

For the purpose of this study, the shaft was described using a local shaft coordinate system compatible with the NED convention, in which the horizontal axes define the local transverse plane of the shaft and the vertical axis is directed downward along the shaft. The UAV attitude is expressed in its body-fixed FRD frame, where the axes correspond to forward, right, and down directions. Therefore, the UAV body frame should not be interpreted as a global coordinate system, but rather as a moving frame rigidly attached to the aircraft.

The six cameras are rigidly mounted to the UAV frame and directed horizontally towards the shaft lining. Their orientations with respect to the UAV body frame are fixed and differ mainly by the yaw mounting angle. As previously mentioned, the first camera is rotated by 30° about the UAV down axis, while each subsequent camera is rotated by an additional 60°. Consequently, the exterior orientation of each image is obtained from the UAV pose in the shaft coordinate system and the fixed lever-arm and boresight transformation between the UAV body frame and the corresponding camera frame. In this sense, the roll, pitch, and yaw angles of the UAV are related to the angular elements of camera exterior orientation, but they are not directly identical to the photogrammetric ω, ϕ, and κ angles unless the same axis convention, rotation order, and camera-frame definition are explicitly adopted.

For a given camera i, its projection center in the shaft coordinate system can be expressed as

$$\mathbf{C}i^S = \mathbf{p}_{UAV}^S + R_B^S \mathbf{t}_{C_i}^B, \quad (1)$$

where $\mathbf{p}_{UAV}^S$ is the UAV position in the shaft coordinate system, R_B^S is the rotation matrix from the UAV body frame to the shaft coordinate system, and $\mathbf{t}C_i{}^B$ is the fixed lever

arm from the UAV body origin to the center of camera i, expressed in the body frame. The corresponding camera orientation is obtained as

$$R^S_{C_i} = R^S_B R^B_{C_i}, \tag{2}$$

where $R^B_{C_i}$ describes the fixed mounting orientation of camera i with respect to the UAV body frame.

The collinearity equation [26–28] (Equation (3)) establishes the collinearity relationship between the vector inside the camera that connects the center of projections and the image point in the photo, and the vector that connects the center of projections with the shaft tubbing point. The xy position of points in the photo is determined by the function of the position of the point in the XYZ coordinate system, based on the internal orientation elements c_k, x_0, y_0 of the camera and linear external orientation elements (terrain coordinates of the projection center X_0, Y_0, Z_0) and angular elements (in the form of a rotation matrix $[r_{11} \ldots r_{33}]$).

$$\begin{aligned} x &= c_x - f \cdot \frac{r_{11}(X - X_0) + r_{21}(Y - Y_0) + r_{31}(Z - Z_0)}{r_{13}(X - X_0) + r_{23}(Y - Y_0) + r_{33}(Z - Z_0)} \\ y &= c_y - f \cdot \frac{r_{12}(X - X_0) + r_{22}(Y - Y_0) + r_{32}(Z - Z_0)}{r_{13}(X - X_0) + r_{23}(Y - Y_0) + r_{33}(Z - Z_0)} \end{aligned} \tag{3}$$

The process of photo-network alignment entails the identification of the most probable external orientation of photographs, which is typically in close alignment with or identical to the orientation observed during the moment of image capture. This process involves the determination of the coordinates of ground control points with respect to a defined reference system. The first element to consider is the internal camera orientation parameters. Secondly, the shaft tubing data coordinates of the photographed control points are to be included. The third point pertains to the measurement of the image coordinates of the photographic points, in conjunction with the subsequent matching results, which correspond to the image coordinates of the control points. The captured approximate elements of external orientation are as follows: the initial stage of the calculation is the mutual orientation of successive images in the sequence (or adjacent in space), by adding corresponding beams to the initial beam. This process generates a model of the area, with an approximate scale and position relative to the coordinate system defined by the approximate elements of image orientation. In the second stage, the model is integrated into the object (shaft tubbing) and aligned. In the case of images captured within a shaft environment during manually controlled trials with external reference point, the internal orientation components of the camera are determined through a process of calibration. At stage of manually controlled flights, the external orientation elements were not measured. However, the method has the potential to determine them approximately based on the central vertical and the IMU unit. Absolute orientation is derived from the measurement of control points' previously scanned by a TLS scanner. However, during captures incorporating a UAV stabilization system, every image was geotagged based on the UAV's position in the moment of capturing. UAVs position data was then recalculated for every camera separately. Calculation based on extrinsic parameters determined during calibration in Section 2.3.

2.5. Reference and Laser Scanning During Manually Controlled Trials with External Reference Points

For this measurement attempt focused on flight in regular airflow conditions for approximately 50 m in height, a methodology similar to that used in the authors' previous work on photogrammetric measurements in the rock salt interval of the SW-4 mineshaft [29]

was applied. In brief, a series of photogrammetric targets were installed along a fixed vertical interval of the cast-iron tubbing lining. These targets were then precisely measured (with 3.5 mm accuracy) using laser scanner to establish a georeferenced point cloud for later image alignment and 3D reconstruction. All reference points were installed at west half of GG-1 mineshaft. A total of 24 points were placed from 1st to 30th tubing ring reaching a total vertical distance of 45 m. A detailed view of the installed targets within the cast-iron lining is presented in Figure 9 below.



Figure 9. Photograph of reference point placed in installation hole in cast-iron tubing lining segment.

Once the reference network was established, the 2nd tubing column in GG-1 mineshaft was scanned at 50 m interval using a terrestrial laser scanner (TLS) to generate a reference model and determine the coordinates of each reference point. Within each 50 m section, four scans were acquired to produce a well-aligned point cloud. The final 3D model obtained from TLS comprised over 250 million points. An excerpt of the TLS scan is shown in Figure 10, where exemplary reference point is clearly identifiable. The coordinates of each well-defined point were used to accurately orient and scale the photogrammetric 3D model generated from UAV imagery. As illustrated in Figure 10, the main limitation of static TLS scanning is apparent: the greater the distance from the scanner, the larger the gaps in the rear wall of the tubing segment.

Despite this limitation such a laser scan is sufficient for accuracy analysis that will be presented in Section 3.

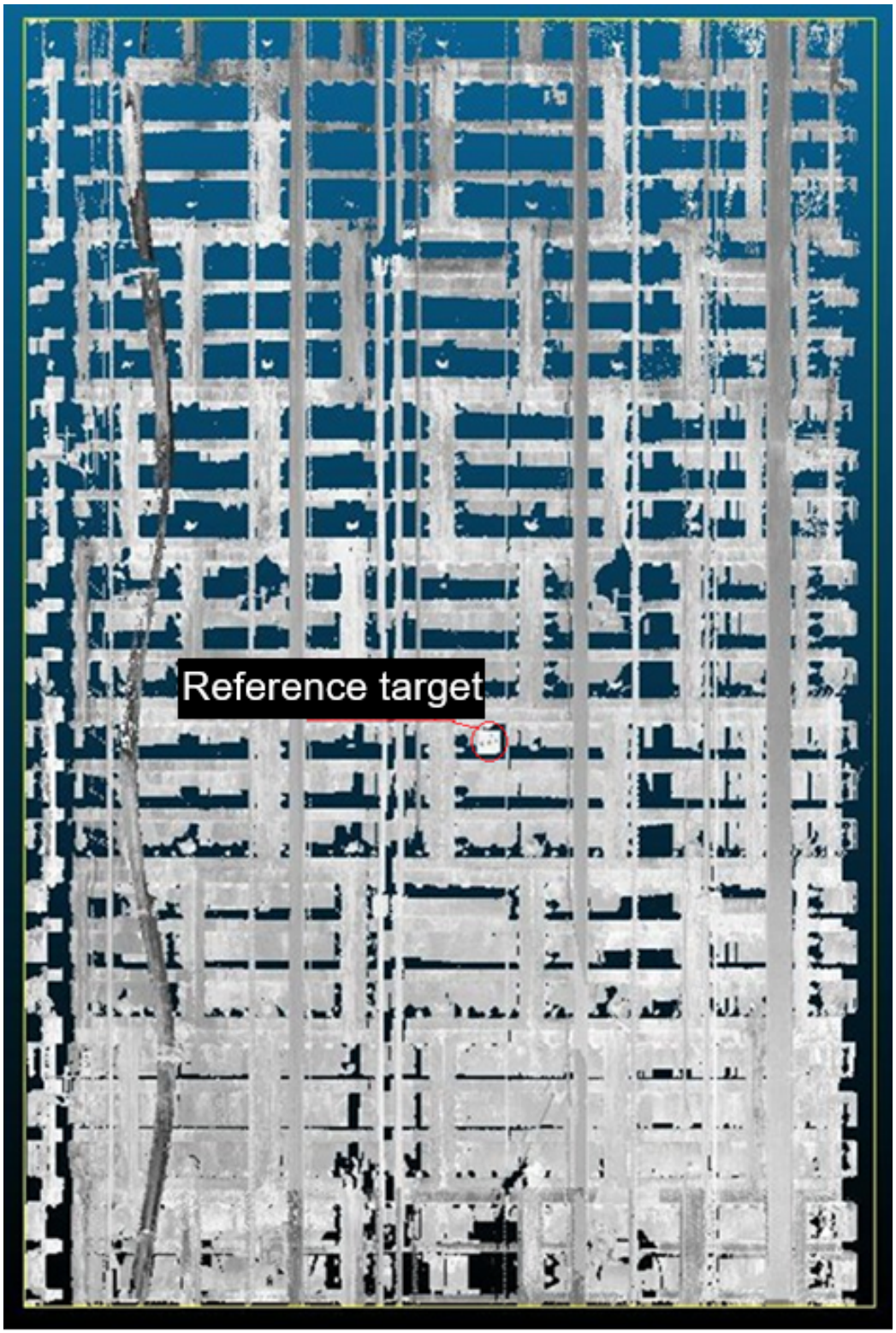

Figure 10. Part of laser scan of 2nd tubing column in GG-1 mineshaft with highlighted reference point.

2.6. Flight Conditions and Parameters in Manually Controlled Trials with External Reference Points

The primary flight, which provided the data used in this study, covering the section from the bottom starting point at 986 m below ground level (b.g.l.) to 936 m b.g.l. The GG-1 mineshaft currently serves primarily as an intake ventilation shaft, with measured air velocities exceeding 8 m/s. Notably, the airflow was directed vertically downward, exerting a considerably greater influence on the UAV's stability compared to typical operations. While regular

UAV flights are occasionally conducted in air velocities exceeding 8 m/s, such winds are never oriented directly downward [30]. The flight was executed without any form of position stabilization. During this test, the drone was controlled manually in real time via a remote controller by one of the authors. Despite his extensive UAV piloting experience, the severe flight conditions rendered it impossible to maintain a stable trajectory or constant velocity. The constant downward airflow significantly increased the challenge of precise maneuvering, underscoring the operational difficulty of UAV missions in deep vertical mining environments. Considering such conditions, shape of UAV and general conception to use central vertical (steel line placed in the center of the mineshaft) becomes much more meaningful. The UAV used in this part of study remained in the early development phase and was not yet equipped with several key components necessary for safe, extended-duration flights. In particular, it lacked horizontal stabilization and vertical odometry. For safety reasons, the flight was therefore conducted with the UAV secured by a rope held by an operator positioned in a shaft bucket located above the UAV. This rope served solely as an emergency measure and did not influence the UAV's flight performance at any stage of the flight. A photograph captured from the shaft bucket during the described flight is shown in Figure 11.



Figure 11. Photo taken during UAV flight from shaft's bucket.

The main flight concluding manually controlled trials with external reference points lasted approximately seven minutes and covered a distance of 50 m. The primary area of investigation during this trial was the second tubing column in the GG-1 mineshaft, which extends to a height of 45 m. Due to strong downward airflow and safety measures, the UAV operated at a lower velocity than anticipated for subsequent trials. The mean resultant speed did not exceed 0.5 m/s, leading to a higher than required vertical overlap of the acquired images. The UAV captured over 1200 photographs at a frequency of 2 Hz per camera, yielding more than 200 GB of visual data. Despite these challenging aerodynamic

conditions, the UAV maintained a stable position, with roll and pitch deviations ranging between –2° and +3°. Rotation measurements obtained from the (IMU) are presented in Figure 12. The estimated angles present a direct estimation of UAV pose from the EKF module in the autopilot. Angle controls are shown as Setpoints. It is worth mentioning that horizontal rotations that can be observed in Figure 12 (below) did not influence the quality of the photogrammetric material.

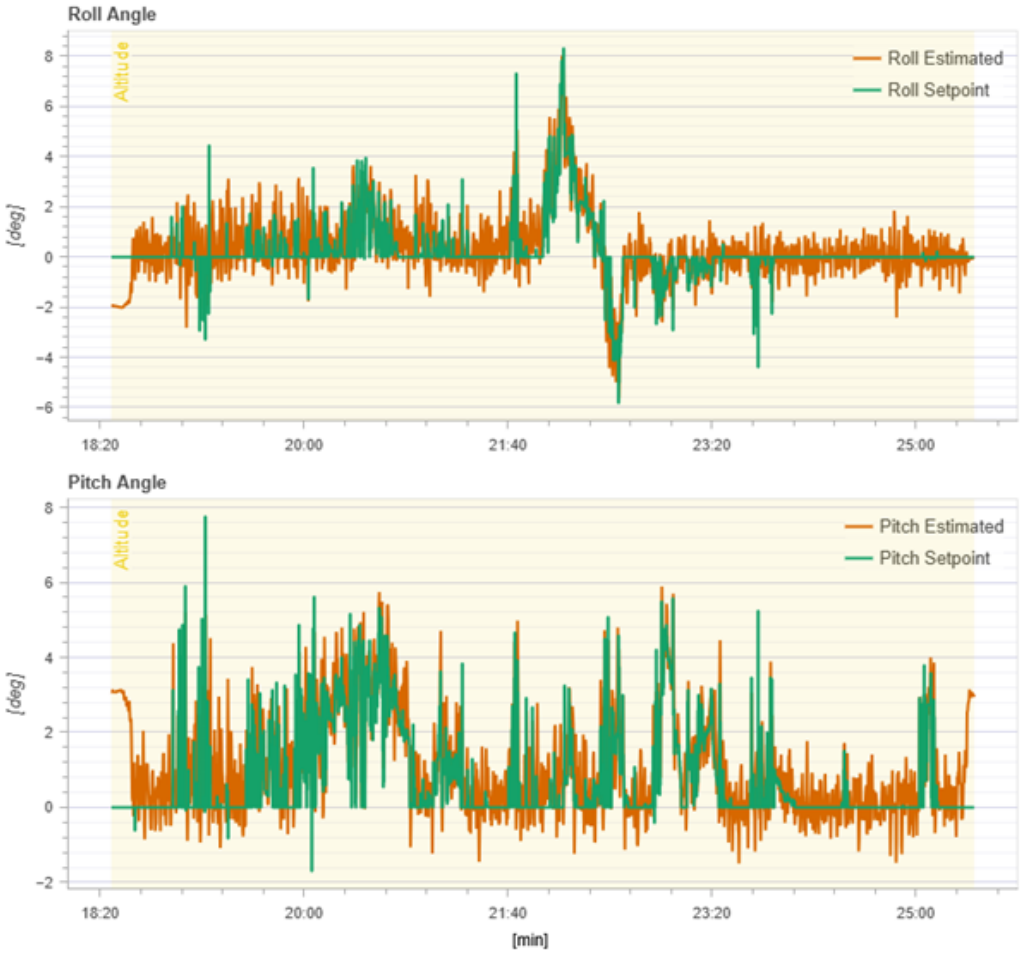

Figure 12. Rotation angles estimated by UAV and control setpoints.

2.7. Stabilized Trials Without External Reference

In time of this research, the GG-1 mineshaft was undergoing installation of the guide rails for the main cage, counterweight, and inspection cage. During the construction works, high-altitude flights could not be conducted at the same depth during each measurement session because the working platform from which the flights were launched was progressively lowered. Therefore, the authors decided to use the connection points between individual rail sections as external reference points for photogrammetric measurements. Each rail section was installed with a precision of 3 mm and was therefore considered suitable as a reference feature for the required inspection accuracy. Moreover flights with stabilization system were launched from the same depth from guide-rope tensioning frame for shaft sinking buckets. The launching frame was placed just above shaft bottom station and is presented below in Figure 13.

The stabilized trials without external reference system consisted of three separate flights focused on collecting data for the autopilot system and identifying the optimal procedure for photogrammetric measurements under real shaft conditions. Two of the three trials covered a vertical distance of approximately 50 m, while the final flight in

stabilized trials without external reference exceeded 100 m. The results of all three trials are presented in Section 3.2.

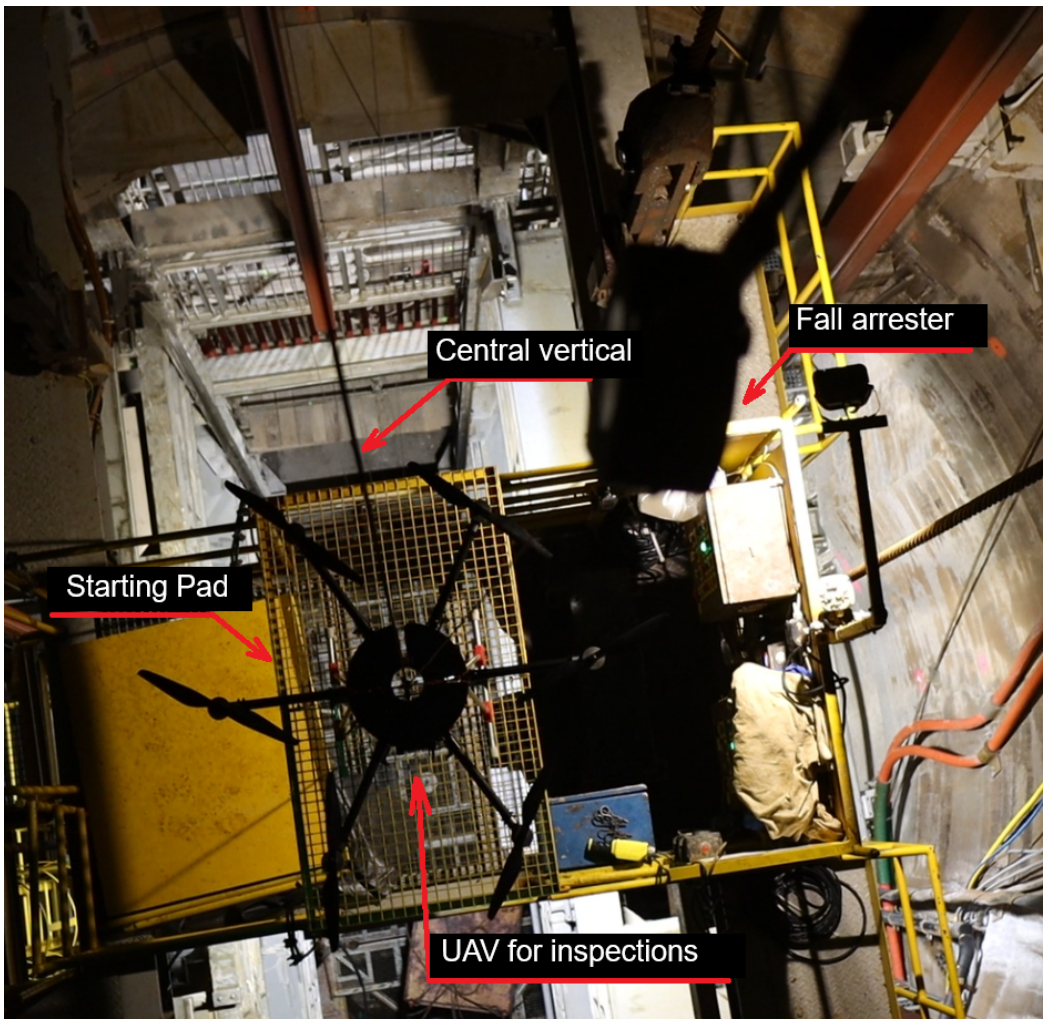

Figure 13. Launching place for stabilized trials without external reference.

The first trial incorporating the developed navigation system ended with the UAV's propeller becoming entangled in the safety line. After more than 40 m of stable flight, the UAV rapidly accelerated vertically, reaching a velocity that exceeded the reeling capability of the fall-arrest system.

The second trial focused on maximizing the amount and quality of photogrammetric data acquired during the flight. To improve horizontal image overlap, the authors exploited the UAV's ability to rotate about the vertical axis during flight. By applying a controlled yaw offset during the downward trajectory, the system acquired the same shaft section from an additional viewing direction. This represents a novel aspect of the proposed methodology, as it improves photogrammetric acquisition geometry without adding cameras. The UAV ascended with the first camera oriented toward the northern guide rail of the main cage and then descended after being rotated by 30° in yaw. This approach improved image overlap, viewing geometry, and overall 3D model quality. However, the flight was conducted in altitude mode, relying only on horizontal angles stabilization and vertical speed control based on barometer and IMU readings. From the early stage of the ascent, the sensor responsible for measuring vertical displacement was inactive. As later determined, it had been disconnected from its carrier board—most likely due to vibrations. The sensor has been reconnected and secured mechanically to prevent this problem in the future. In the absence of this key sensor,

conducting a high-altitude flight was not the safest approach. Nevertheless, even without precise internal vertical reference, the flight provided more than 3000 photographs, including images acquired with a 30° yaw offset between ascent and descent.

The third trial was conducted after redesigning the casing of the vertical displacement sensor to improve its durability. During the first 95 m of flight, the UAV maintained an acceptable horizontal position without exerting excessive pressure on the central steel vertical rope. However, during the final 5 m of the flight, the UAV horizontal position began to drift. Initially, this horizontal motion was compensated for, and the UAV remained stable, then suddenly moved rapidly westward toward the bucket guide rope. The displacement of the central vertical greatly exceeded the assumed limit of 15 cm, and the operator decided to terminate the flight in order to prevent a collision. The final moment before the emergency shutdown of the UAV is shown in Figure 14.

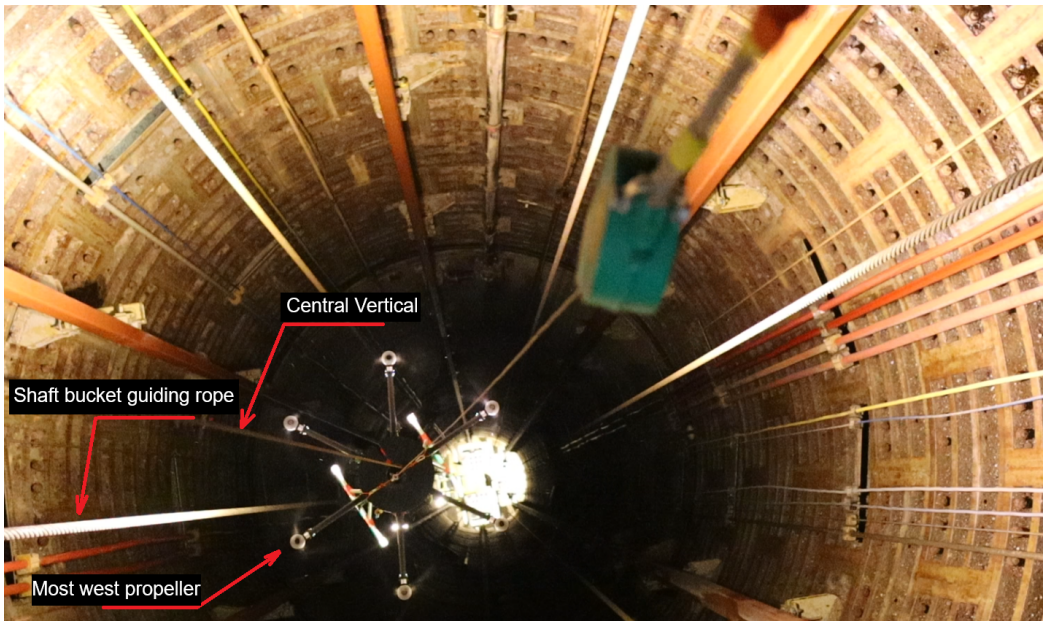

Figure 14. UAV during last trial in the last moment before emergency shutdown.

Although re-arming the UAV after the emergency shutdown was technically possible, it was not considered safe, as the lack of a stable position estimate and unknown sensor biases could have led to incorrect flight behavior. Consequently, this flight provided data only from the upward trajectory, and acquiring photographs with the planned 30° yaw offset during descent was not possible.

3. Results

This chapter presents the results of more than two years of research, during which the UAV underwent continuous development. Therefore, two main groups of results should be distinguished: manually controlled trials using an external reference network and stabilized trials conducted without an external reference network. The first part presents the results of UAV flights in the GG-1 mineshaft, performed using a set of three cameras and without a dedicated stabilization system. In this case, however, an external reference network, described in Section 2.6 was used for spatial referencing and validation. The second part focuses on UAV flights with dedicated stabilization system without external reference. In this case all presented data were processed solely on the UAV's internal reference. It should be emphasized that the validation results obtained for these two approaches are not directly comparable, as they were based on different experimental assumptions, reference conditions, UAV configurations, and stages of platform development.

3.1. Manually Controlled Trials with External Reference Points

This chapter presents the results of manually controlled trials with external reference points across multiple dimensions. It begins with a description of the visual representations of the surveyed objects, given their utility for inspection. Secondly, the accuracy of the photogrammetric model was compared to the laser scanning model for the purpose of validation.

3.1.1. Visual Representation of Measured Object

Considering that the UAV was still under development and, as noted earlier, lacks several key features required for long, stable, and fully autonomous flights, the main trial nonetheless yielded a substantial number of photographs. These images enabled the reconstruction of a well-oriented and accurately scaled photogrammetric 3D model of the second tubing column.

Photogrammetric processing was performed using Agisoft Metashape [31]. The generation of a dense point cloud consisting of over 250 million points required approximately 8 h on a mid-range laptop workstation equipped with an AMD Ryzen 7 4800H processor, 24 GB of RAM, and a discrete NVIDIA GeForce GTX 1660Ti GPU with 6 GB of dedicated memory. In this case, the "High" quality setting with mild depth filtering was applied. Using the "Ultra High" quality setting resulted in a dense point cloud of nearly 1 billion points, with a processing time of approximately 10 h on a high-end desktop workstation equipped with an Intel Core i9-14900K CPU, 128 GB of RAM, and a NVIDIA GeForce RTX 4090 GPU with 24 GB of dedicated memory. Image alignment was performed using 1000 key points per megapixel, 10,000 tie points, and guided image matching. The adopted parameters were selected empirically through preliminary processing trials as a compromise between reliable image alignment, reconstruction quality, and computational efficiency. Since the main objective of the study was to validate the proposed UAV-based inspection workflow in a challenging underground environment, exhaustive optimization of the photogrammetric processing parameters was outside the scope of this work. The time required for three-dimensional model generation can be significantly reduced by employing professional, high-performance computing hardware. Furthermore, the use of internal reference data in Agisoft Metashape substantially simplifies and accelerates the computational process. With a high-end workstation and carefully selected computational settings, the generation of an inspection-grade three-dimensional model can reasonably be expected to be completed within approximately 3 h, which corresponds to the duration of current inspection procedures conducted in the GG-1 mine shaft. It should be emphasized that the proposed solution is intended to enhance existing inspection practices rather than to replace them. To enhance clarity, an 8 m section of this model is presented in Figure 15, with a detailed close-up highlighting structural features of an individual tubing segment shown in Figure 16.

The photogrammetric 3D model presented in Figures 15 and 16 consists of over 250 million points. At this level of resolution, several structural elements of the shaft can be clearly distinguished, including pipelines, survey targets, cable routes, and working platform ropes. Furthermore, with sufficient magnification, it is possible to identify the tubing type, year of production, painted segments, and even individual ring numbers [32]. Given the primary assumption that this UAV is meant to be employed mainly for safety inspections, the quality of the dense point cloud model and the detailed representation of the tubing lining can be considered fully adequate for this purpose. The blank areas visible Figure 15 result from the single-perspective image acquisition; objects located closer to the UAV obstruct features situated behind them, preventing their reconstruction. This represents the principal limitation of the method in terms of 3D model generation. However, within the unique environment of a mineshaft, factors such as flight safety, equipment

flexibility, and operational efficiency are of greater importance than the loss of a few percent of the field of view.

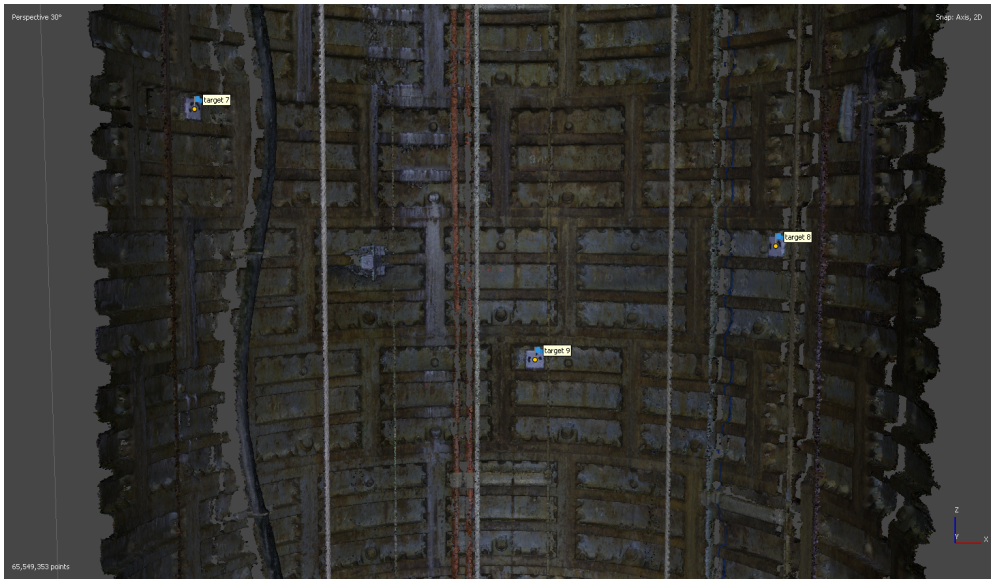

Figure 15. Part of photogrammetric 3D model (dense point cloud) generated from single flight in manually controlled trials with external reference points.



Figure 16. Single tubing segment close-up with highlighted details (marked with red circle).

3.1.2. Accuracy Validation of Results from Manually Controlled Trials with External Reference Points Based on TLS Scan

As previously noted, the entire second tubing column in the GG-1 mineshaft was scanned using a professional terrestrial laser scanner FARO Focus 3D. A distance of 45 m

was covered with four individual scans. As illustrated in Figure 10, gaps in the rear tubing wall are visible. This scan was originally conducted by KGHM ZG Rudna mine for cage rail straightness assessment and was therefore not focused specifically on the tubing lining. Nevertheless, the lower portions of each scan were accurately represented and could be utilized for validation purposes. For point cloud alignment and validation, CloudCompare [33] software was employed (version 2.3.1). Alignment was performed using reference points visible in Figures 9 and 10. Following alignment, the cloud-to-cloud distance was calculated using the M3C2 (Multiscale Model-to-Model Cloud Comparison) algorithm [34]. The results of this validation are presented in Figure 17, with the corresponding histogram shown in Figure 18.

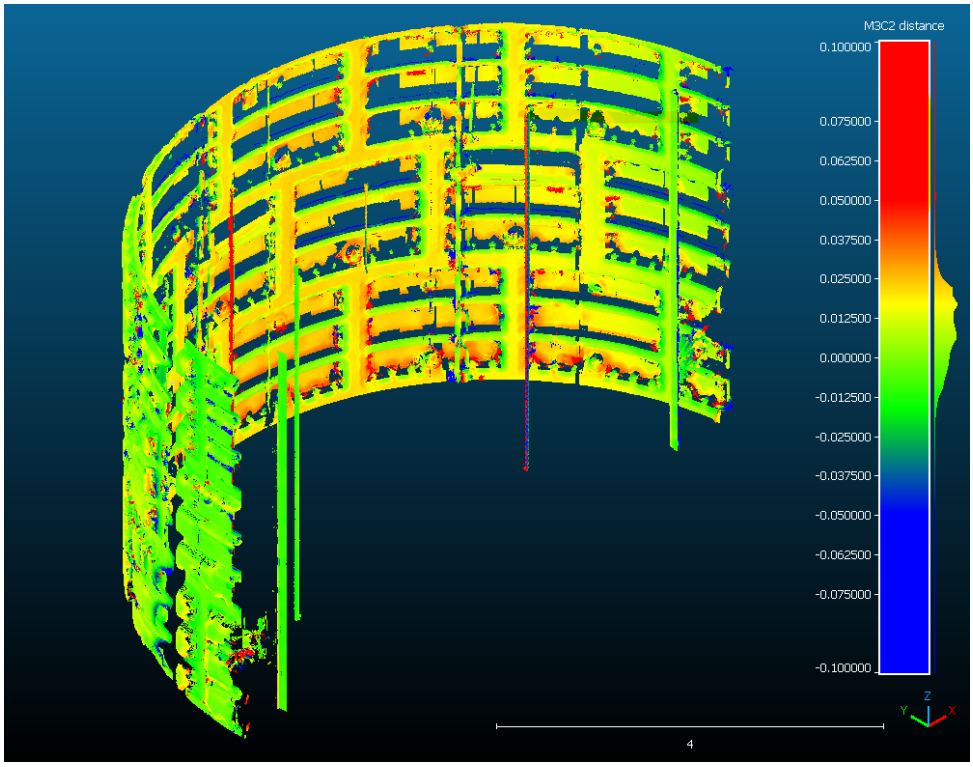

Figure 17. Cloud-to-cloud distance calculated with M3C2 algorithm.

The M3C2 scale parameters are expressed in the coordinate units of the processed point clouds. The normal scale was set to 0.132808, while the projection/search scale was also set to 0.132808. The maximum search depth along the normal direction was set to 0.664040. The normal estimation settings included a minimum scale of 0.066404, a step of 0.066404, and a maximum scale of 0.265616. Core point subsampling was disabled, and median-based projection was not used. The histogram presented in Figure 18 is based on signed M3C2 distances only. No confidence interval-based filtering or significant-change classification was applied to the presented distance distribution. No additional global registration error or precision maps were introduced into the M3C2 computation.

Given that this UAV system is designed primarily for inspection rather than high-precision geodetic measurements, an accuracy range of −5 cm to +5 cm is considered sufficient for its intended applications [35]. Importantly, over 90% of the measured values fall within −3 cm to +3 cm, which demonstrates that the system delivers a level of precision comparable to certain cost-effective hand-held scanners currently used in industrial environments. This level of accuracy is adequate for detecting structural irregularities, assessing general condition, and supporting routine monitoring tasks in a mineshaft.

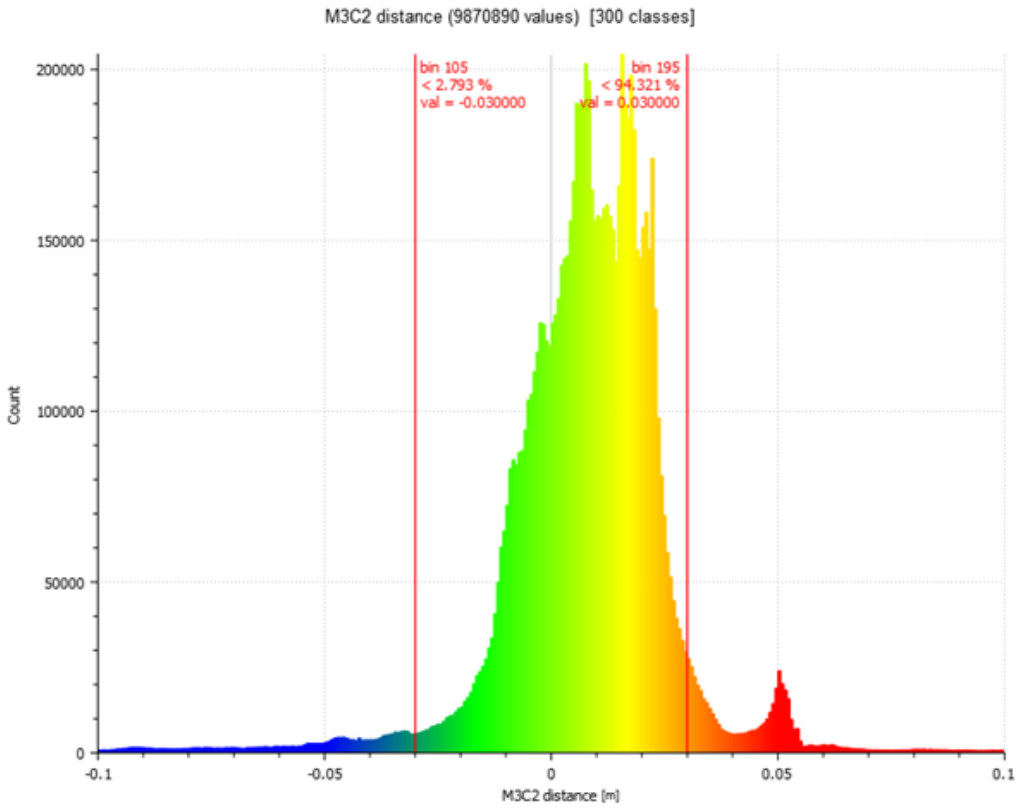

Figure 18. Cloud-to-cloud distance calculated with M3C2 algorithm histogram.

In addition to the general cloud-to-cloud distance computation, a reference point alignment was performed between the terrestrial laser scan and the photogrammetric model. With the exception of two points that were only marginally visible in the laser scan (targets 4 and 13 from Table 4). Those points were excluded from photogrammetric calculations. The accuracy of the photogrammetric model across the entire measured object corresponded well with the results obtained from the cloud-to-cloud analysis. The distance error between the photogrammetric model and the laser scan values ranged from 1 cm to 5 cm. Comparison between scanning and photogrammetric models in fixed reference points are presented in Table 4.

Table 4. Reference point alignment between laser scan and photogrammetric model. Excluded points are marked in color red.

Marker	X Error [m]	Y Error [m]	Z Error [m]	Rmse [m]
target 1	0.0051	0.0077	0.0006	0.0093
target 2	0.0059	0.0122	0.0136	0.0192
target 3	−0.0104	−0.0207	−0.0133	0.0267
target 4	−0.1004	−0.4019	−0.0468	0.4169
target 5	−0.0125	−0.0330	−0.0041	0.0356
target 6	−0.0394	−0.0365	−0.0485	0.0724
target 7	−0.0013	−0.0322	−0.0120	0.0344
target 8	−0.0092	−0.0229	−0.0096	0.0265
target 9	−0.0211	−0.0507	−0.0181	0.0579
target 10	−0.0237	−0.0222	−0.0122	0.0347
target 11	−0.0119	−0.0418	−0.0053	0.0438
target 12	−0.0159	−0.0430	−0.0510	0.0686
target 13	−0.1407	−0.4313	−0.0036	0.4537
target 14	−0.0001	−0.0371	−0.0165	0.0406

Table 4. *Cont.*

Marker	X Error [m]	Y Error [m]	Z Error [m]	Rmse [m]
target 15	−0.0016	−0.0533	−0.0110	0.0544
target 16	−0.0136	−0.0408	−0.0520	0.0675
target 17	−0.0103	−0.0177	−0.0117	0.0236
target 18	−0.0067	−0.0185	−0.0027	0.0199
target 19	−0.0037	−0.0309	−0.0104	0.0328
target 20	Hidden from view in photogrammetric model			
target 21	−0.0124	−0.0199	−0.0097	0.0253
target 22	0.0037	−0.0140	−0.0047	0.0152
target 23	−0.0028	0.0163	0.0024	0.0167
target 24	−0.0015	−0.0015	0.0013	0.0025
σ	0.0107	0.0196	0.0172	0.0198

Additionally, the alignment between the photogrammetric three-dimensional model and the laser scan was evaluated for a single tubing ring. The assessment was performed using the cloud-to-cloud (C2C) absolute distance algorithm [36], with a high-contrast scalar field applied to visualize the differences between the aligned point clouds. The results are presented in Figure 19.

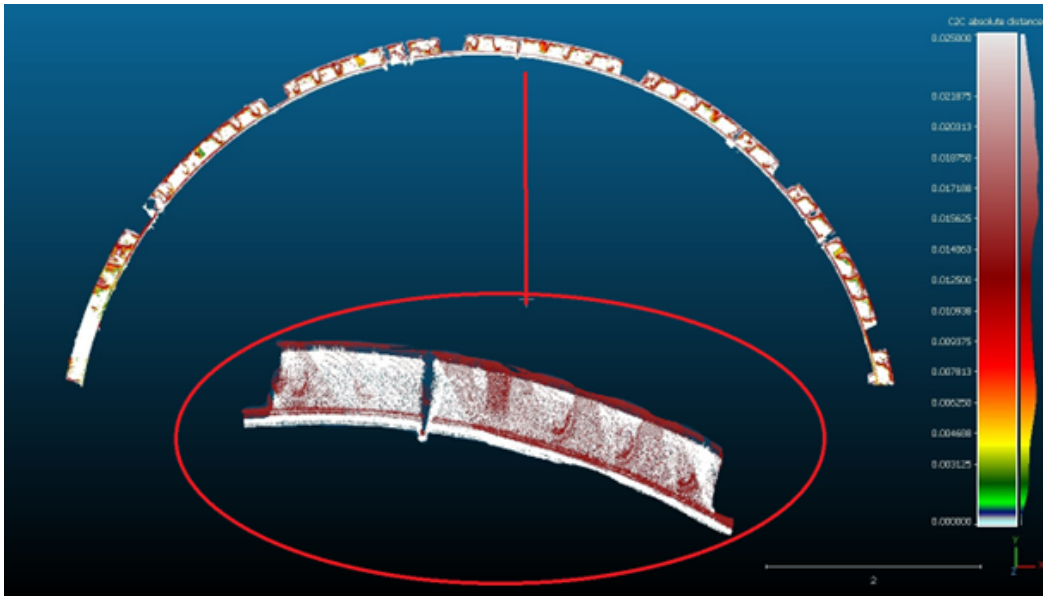

Figure 19. Alignment of photogrammetric 3D point cloud with laser scan.

As shown in Figure 19, the laser scan (visualized using the high-contrast scalar field) exhibits a slightly larger spatial extent than the photogrammetric point cloud (displayed without color information). However, it should be emphasized that both models are geometrically proportional. Distances calculated between the point clouds are consistent with the values obtained from the M3C2 comparison conducted in CloudCompare software. In both analyses, the distances between the models remain within an accuracy threshold of 2.5 cm, indicating a high level of geometric agreement.

3.2. Stabilized Trials Without External Reference

This section describes underground UAV flights featuring tests with the custom designed navigational sensor suite and positioning system. For clarity, each trial is described separately, as the flights differed substantially from one another. Every flight conducted

in the final trials shared similar wind conditions of approximately 5 m/s downward turbulent flow.

3.2.1. First Flight

As mentioned previously, the first flight focused on testing the stabilization system based on a central vertical in an underground environment for the first time and generating a 3D model without any external reference. The models and analyses presented below, for the first trial, correspond to a vertical distance of 25 m. Although the measured distance was approximately 45 m from the UAV starting point to the moment of its sudden uncontrolled upward motion, which resulted in entanglement in the safety line, the provided data was used to reconstruct 25 m. The navigation system assigned the position of the UAV's CoG in the local NED frame to each photograph. This information was then recalculated separately for the position of each camera. For the photogrammetric calculations, only the XYZ coordinates of each photograph were considered. Unfortunately, incorporating yaw, pitch, and roll angles into the calculations resulted in incorrect scaling and orientation; for example, the shaft diameter was reconstructed as only 6 cm. Allowing the photogrammetric software to estimate the extrinsic angles of each photograph resulted in a correctly oriented and scaled point cloud consisting of over 150 million points. During this flight, the initial UAV velocity was approximately 1.5 m/s, while the maximum velocity reached nearly 4 m/s shortly before the UAV became entangled in the safety line. With the image acquisition frequency limited to 2 Hz, the higher flight velocity resulted in reduced image overlap and, consequently, lower model quality. The difference in visual quality between the lower- and higher-velocity sections of the flight is shown in Figure 20.

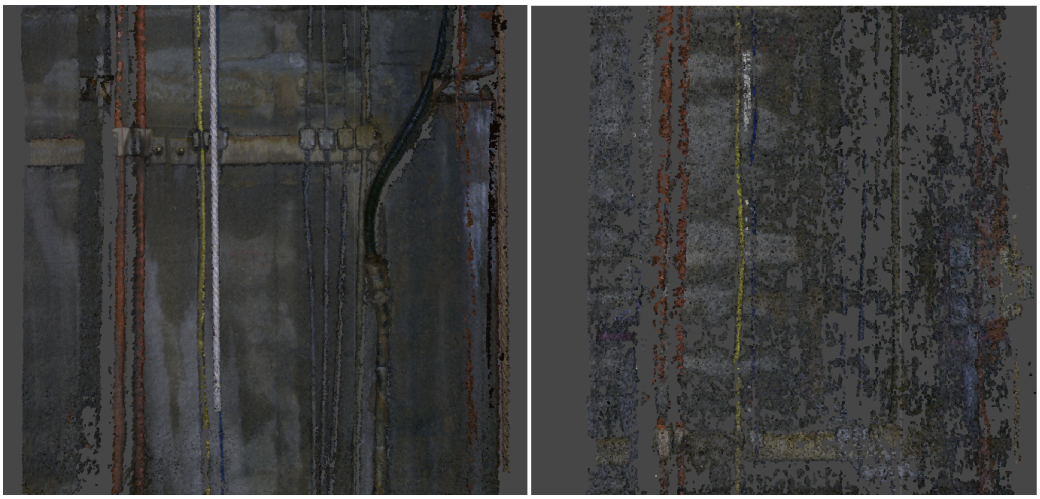

Figure 20. Difference in visual quality of 3D model based on velocity. Low velocity—below 1 m/s (**left**); high velocity—above 3 m/s (**right**).

As presented in Figure 20, the difference is significant, especially considering details such as bolts and less distinguishable cables. However, regardless of velocity, photographs matched into a well oriented and proportional point cloud based only on internal reference.

3.2.2. Second Flight

The second trial, due to the absence of data from the vertical displacement sensor, focused primarily on acquiring the best possible photogrammetric data. To achieve this, the returning downward flight was performed with a 30° yaw offset to maximize image overlap and improve viewing geometry. This approach resulted in a considerable improvement in the visual quality of the point cloud. The difference in visual quality between the first and second trials is shown in Figure 21. As presented, the difference in the visual

quality of the point clouds is clear. For this comparison, the same single interval of the concrete lining was selected, marked "W214". In both trials, the UAV maintained a stable velocity of 1 m/s in this part of the flight.

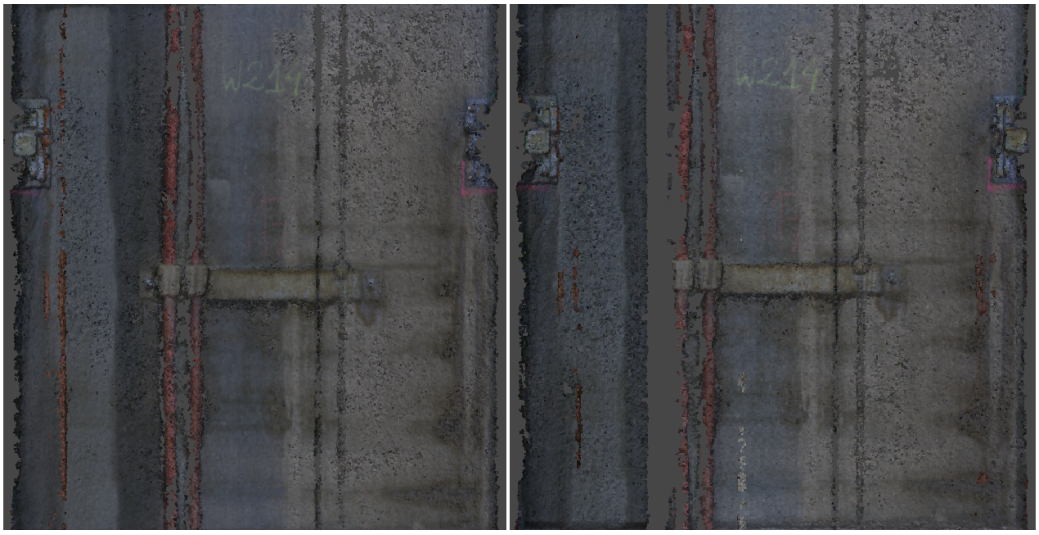

Figure 21. Comparison of visual models quality of second flight with yaw offset (**left**) and second trial without yaw offset (**right**). Vertical velocity of both flights was similar—about 1 m/s.

To quantitatively support the visual comparison, both image sets were processed using the same photogrammetric workflow and compared using tie point statistics, reprojection error, dense cloud density and surface completeness. The analyzed shaft section, corresponding to a single interval of concrete lining, was approximated as a cylindrical surface with a diameter of 7.5 m and a height of 3.5 m, resulting in a reference surface area of 82.47 m^2.

Surface completeness was additionally assessed using cylindrical unwrapped point clouds exported from CloudCompare. Both point clouds were rasterized using a regular 2D grid with a cell size of 0.05 m $\times$ 0.05 m. A grid cell was classified as reconstructed when it contained at least 10 points. This threshold was selected to avoid classifying isolated noise points as reconstructed surface while still preserving local surface gaps.

The yaw-offset acquisition increased tie point density from 3988 to 9648 pts/m^2 and projection density from 10,878 to 28,391 proj./m^2. The average tie point multiplicity also increased from 2.899 to 3.459, indicating improved observation redundancy. Surface completeness increased from 95.22% to 98.41%, and the largest continuous gap was reduced from approximately 0.96 m^2 to 0.56 m^2. However, the RMS reprojection error increased from 1.282 pix to 1.403 pix. Therefore, the yaw-offset acquisition improved reconstruction support, observation redundancy and spatial completeness, although it did not reduce the reprojection error. The quantitative comparison and surface completeness analysis is presented in Table 5.

Theoretically, greater image overlap could be achieved by using eight cameras instead of six. However, this solution was limited by the available hardware interfaces of the onboard computing platform. The Auvidea JNX45 carrier board used with the Jetson Orin NX provides two native USB 3 ports and five shared USB 3 ports. The shared interfaces substantially limit the available bandwidth for each camera during synchronous image acquisition. Moreover, the authors did not identify a carrier board available on the market that would provide at least eight independent USB 3 interfaces suitable for this application. The use of additional cameras and a more capable onboard computing platform would also increase the weight of the photogrammetric module and the power consumption of the UAV. Changing the lenses to a shorter focal length, for example, 6 mm, was also not considered

optimal, as it would increase lens distortion and reduce the lens aperture from F1.4 to F1.8. During the selection of cameras and lenses, the authors aimed to obtain the shortest possible exposure times while maintaining sufficient image quality. Therefore, the selected photogrammetric equipment was considered an appropriate compromise between image overlap, image quality, take-off weight, and power consumption. Moreover, performing the downward flight with a yaw offset proved to significantly improve the visual quality of the point cloud by virtually doubling the number of cameras. The point cloud reconstructed from the second trial was generated using only external references, due to absence of vertical displacement sensor readings. The authors intended to use the connection points between cage rail sections instead of dedicated markers. The coordinates of each selected point were obtained from a laser scan. Although this approach certainly resulted in higher errors and lower repeatability than with use of fixed pre-measured reference points, it provided greater flexibility in terms of areas without free access. Moreover, the use of dedicated targets, as in the manually controlled trials, was no longer possible for safety reasons. The targets installed previously had corroded and had to be removed due to the mineshaft's atmosphere. Accuracy validation, using the C2C absolute distance algorithm based on a laser scan, of the model generated in the second trial is presented below in Figure 22 with corresponding histogram in Figure 23.

Table 5. Quantitative comparison of models reconstructed with and without yaw offset.

Parameter	Without Yaw Offset	With Yaw Offset	Change
Photogrammetric reconstruction statistics			
Images/aligned cameras	60/60	156/156	+160.0%
Tie points	328,890	795,599	+141.9%
Projections	897,035	2,341,307	+161.0%
Average tie point multiplicity	2.899	3.459	+19.3%
RMS reprojection error [pix]	1.282	1.403	+9.4%
Tie points per image	5482	5100	−7.0%
Projections per image	14,951	15,008	+0.4%
Tie point density [pts/m^2]	3988	9648	+141.9%
Projection density [proj./m^2]	10,878	28,391	+161.0%
Point cloud points	22,120,971	22,960,306	+3.8%
Dense cloud density [pts/m^2]	268,241	278,419	+3.8%
Surface completeness assessment			
Grid size	472 × 70 cells		–
Cell size	0.05 m × 0.05 m		–
Occupied cells	31,461	32,514	+1053
Empty or weakly covered cells	1579	526	−66.7%
Surface completeness [%]	95.22	98.41	+3.19 pp
Largest continuous gap [m^2]	0.96	0.56	−41.7%

The photogrammetric model from the second trial was oriented and scaled using points manually placed in the photographs at the joints between the guide rail sections. Since these characteristic points were located closer to the shaft center than to the shaft lining, the model was partially extrapolated toward the lining surface. Nevertheless, the accuracy of more than 85% of the points did not exceed 5 cm, which is a sufficient value for inspection purposes.

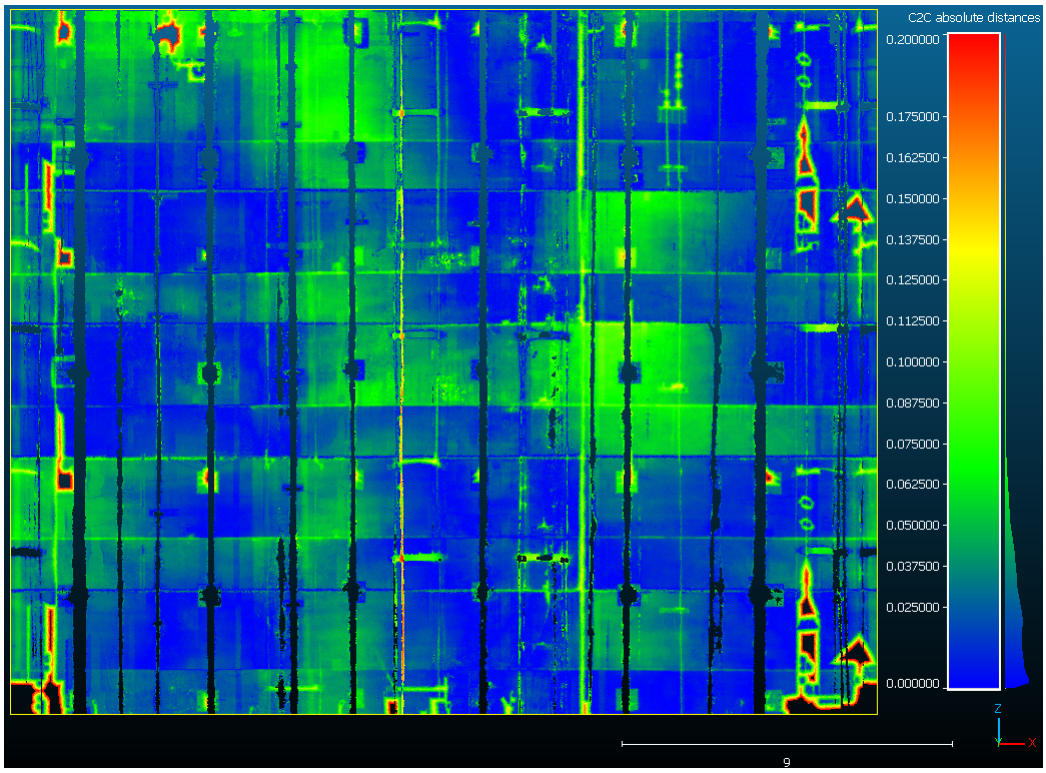

Figure 22. Accuracy validation based on laser scan using C2C absolute distance algorithm of model generated in second trial (unrolled).

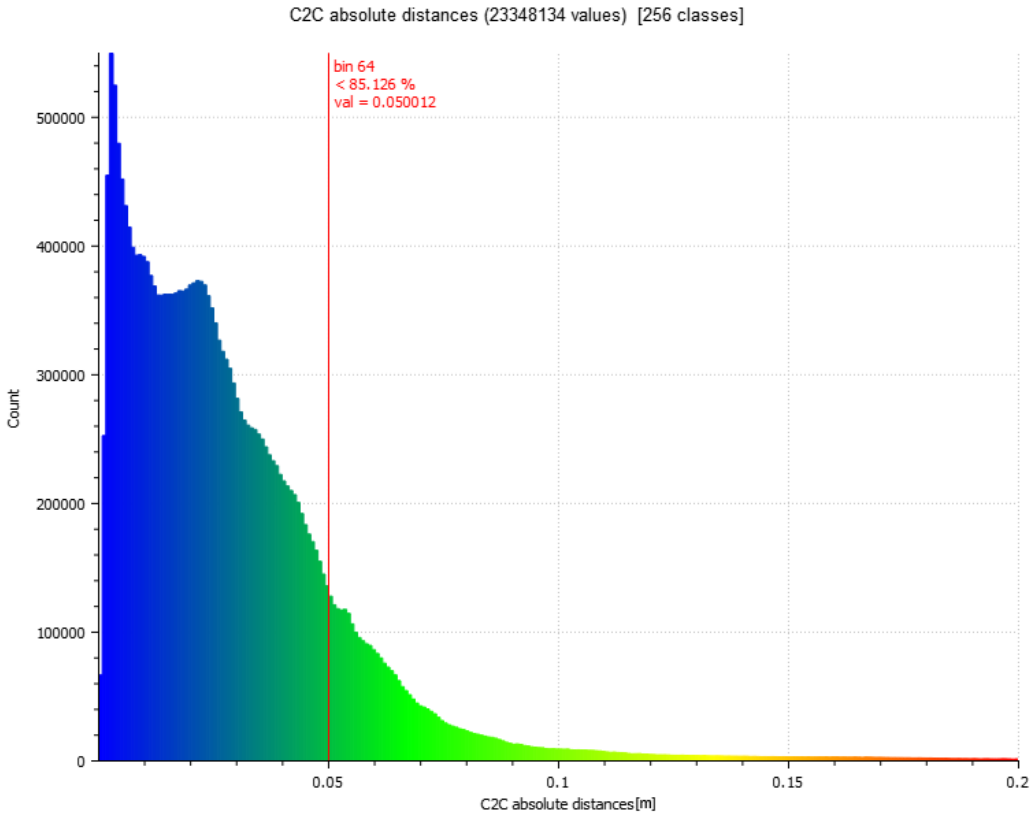

Figure 23. Accuracy validation based on laser scan using C2C absolute distance algorithm of model generated in second trial—histogram.

3.2.3. Third Flight

The third trial aimed to merge flight gathering UAV position data with the conception of yaw rotation offset between upward and downward motion. However, due to the abrupt termination of this flight, only upward motion was registered. Despite the lower visual quality, the point cloud recreated from 1500 photographs, each including individual positions, was generated. The general model of the entire interval inspected in the third trial is presented below in Figure 24. Validation, based on laser scans, of the photogrammetric model of a 30 m high interval, used in validation of tubing and concrete lining created with only internal reference, is presented below in Figures 25 and 26, and the histogram in Figure 27.

The accuracy of the photogrammetric model was further assessed by comparing shaft diameters measured in 2 m vertical intervals with corresponding values obtained from the laser scanning reference cloud. The comparison was performed in two perpendicular directions, N–S and E–W, and the differences represent the deviation of the photogrammetric diameter from the laser scanning reference. Diameter comparisson is presented in Table 6.

The mean discrepancies were 0.076 m and 0.140 m for the N–S and E–W directions respectively, with corresponding RMSE values of 0.101 m and 0.157 m. The photogrammetric model generally underestimated the shaft diameter, particularly in the E–W direction, where higher variability and larger local deviations were observed. These results indicate that the reconstructed model preserved the overall geometry of the shaft, although local metric discrepancies should be considered when interpreting detailed dimensional measurements.

Table 6. Comparison of mineshaft diameters obtained from laser scanning and photogrammetric point clouds. Values are rounded to 0.001 m.

Interval	Height [m]	Depth [m]	Model Type	Diameter [m]		Difference [m]	
				N–S	E–W	N–S	E–W
1	2.0	−1200.12	Laser scan	7.885	7.912	0.069	0.100
			Photogrammetric	7.816	7.812		
2	2.0	−1202.12	Laser scan	7.919	7.915	0.107	0.103
			Photogrammetric	7.812	7.812		
3	2.0	−1204.12	Laser scan	7.925	7.914	0.100	0.103
			Photogrammetric	7.826	7.811		
4	2.0	−1206.12	Laser scan	7.928	8.022	0.114	0.197
			Photogrammetric	7.814	7.825		
5	2.0	−1208.12	Laser scan	7.934	8.101	0.116	0.259
			Photogrammetric	7.818	7.842		
6	2.0	−1210.12	Laser scan	7.806	7.902	−0.018	0.071
			Photogrammetric	7.824	7.831		
7	2.0	−1212.12	Laser scan	7.864	7.922	0.041	0.094
			Photogrammetric	7.824	7.829		
8	2.0	−1214.12	Laser scan	7.900	8.077	0.082	0.253
			Photogrammetric	7.818	7.824		
9	2.0	−1216.12	Laser scan	7.543	7.540	0.103	0.098
			Photogrammetric	7.440	7.442		
10	2.0	−1218.12	Laser scan	7.675	7.642	0.101	0.139
			Photogrammetric	7.573	7.503		
11	2.0	−1220.12	Laser scan	7.709	7.739	0.227	0.287
			Photogrammetric	7.481	7.452		
12	2.0	−1222.12	Laser scan	7.559	7.585	0.053	0.071
			Photogrammetric	7.506	7.514		
13	2.0	−1224.12	Laser scan	7.526	7.588	0.093	0.157
			Photogrammetric	7.433	7.432		
14	2.0	−1226.12	Laser scan	7.606	7.645	0.030	0.075
			Photogrammetric	7.576	7.570		
15	2.0	−1228.12	Laser scan	7.531	7.528	−0.082	0.097
			Photogrammetric	7.613	7.431		
					Mean difference	0.076	0.140
					Median difference	0.093	0.103
					RMSE	0.101	0.157

The photogrammetric model from the third trial, based only on the internal reference provided by the UAV's autopilot, differed from the laser scan by less than 15 cm for more

than 93% of the points within a 30 m high section. Although such accuracy would be unacceptable for geodetic measurements, the authors believe that, for inspection purposes, this result is promising and provides a basis for future studies. Notably, most of the discrepancies were related to horizontal displacement, which can be plainly seen in Figure 26, where the gray area is part of the TLS scan with a greater diameter. This suggests that conducting a complete trial, including a downward flight with a 30° yaw offset, could potentially significantly improve the achieved accuracy. In addition to the main validation, the photogrammetric model from this trial was also evaluated after rescaling during the alignment process. This approach reduced the horizontal discrepancies, which in general did not exceed 5 cm for more than 85% of the points. The validation results for the rescaled model are presented in Figure 28.

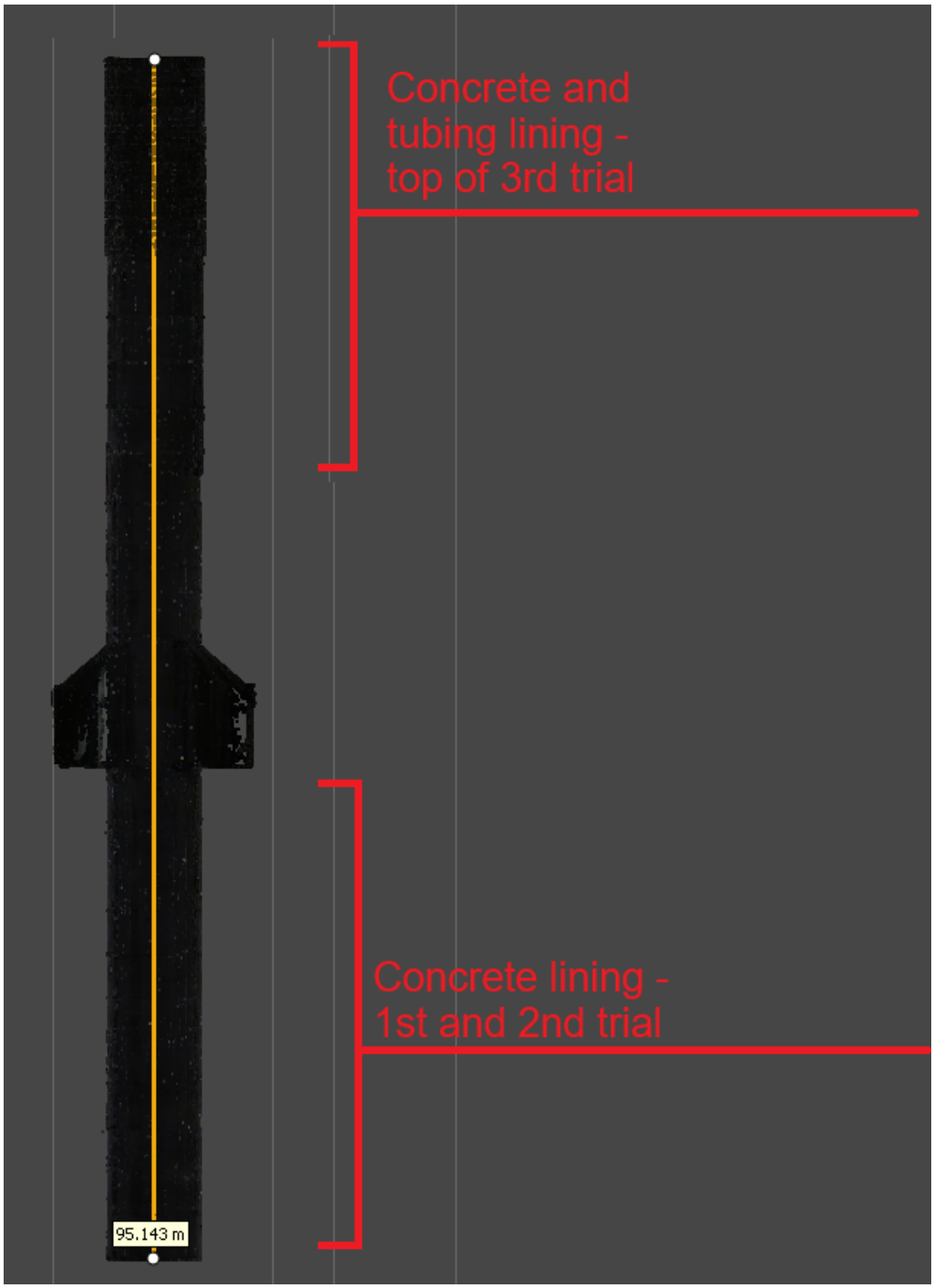

Figure 24. General view of model captured in third trial.

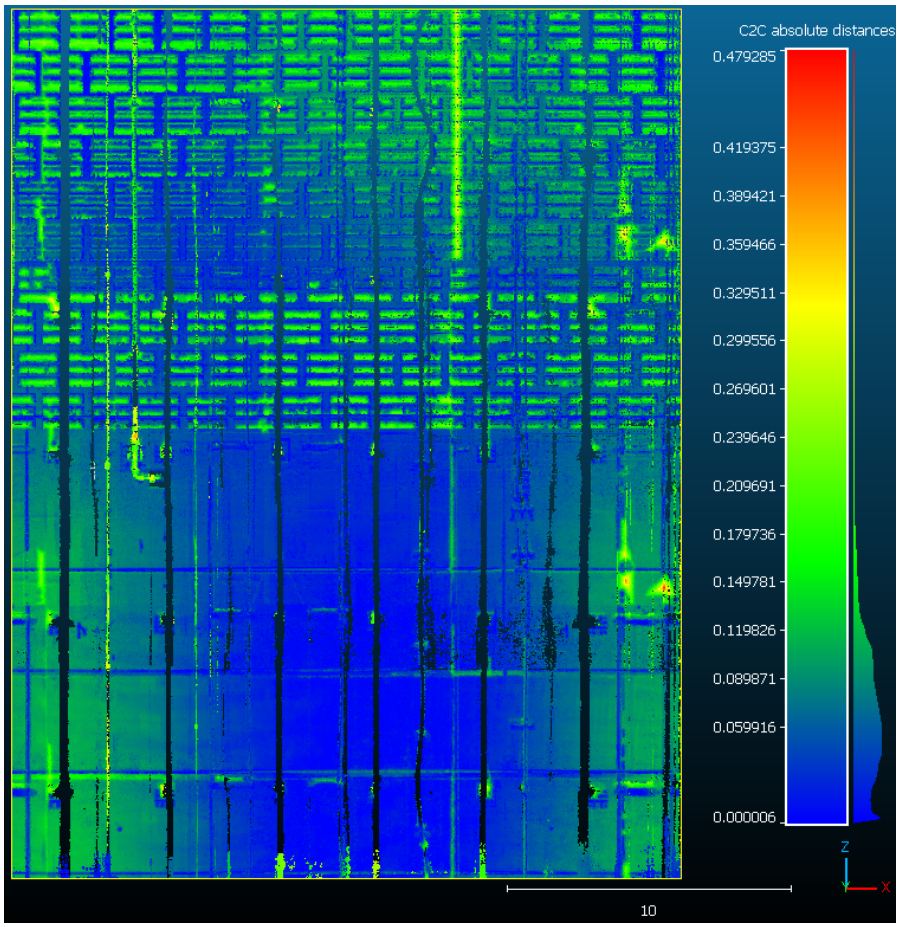

Figure 25. Accuracy validation based on laser scan using C2C absolute distance algorithm of model generated in third trial (unrolled).

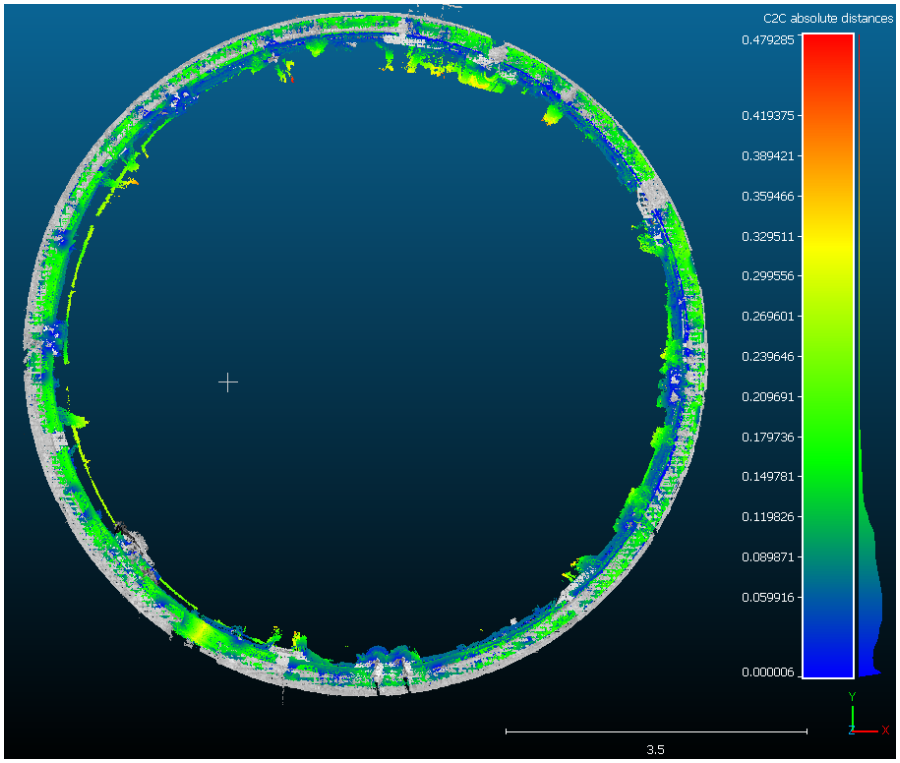

Figure 26. Accuracy validation based on laser scan using C2C absolute distance algorithm of model generated in third trial (planar view).

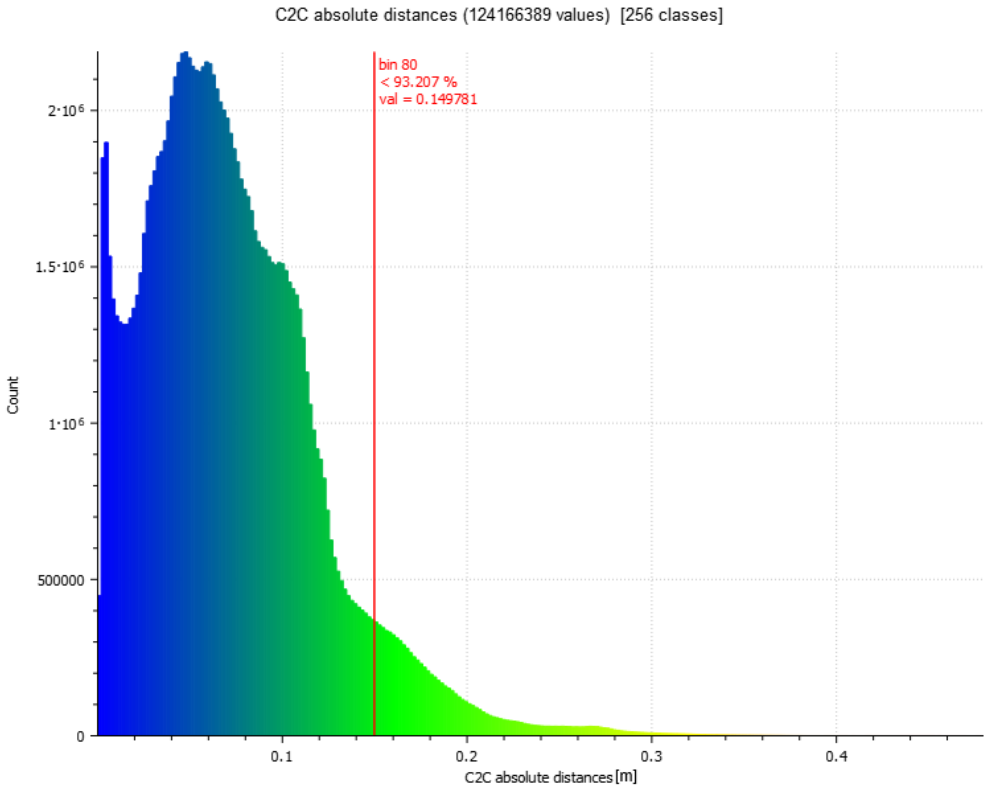

Figure 27. Accuracy validation based on laser scan using C2C absolute distance algorithm of model generated in third trial—histogram.

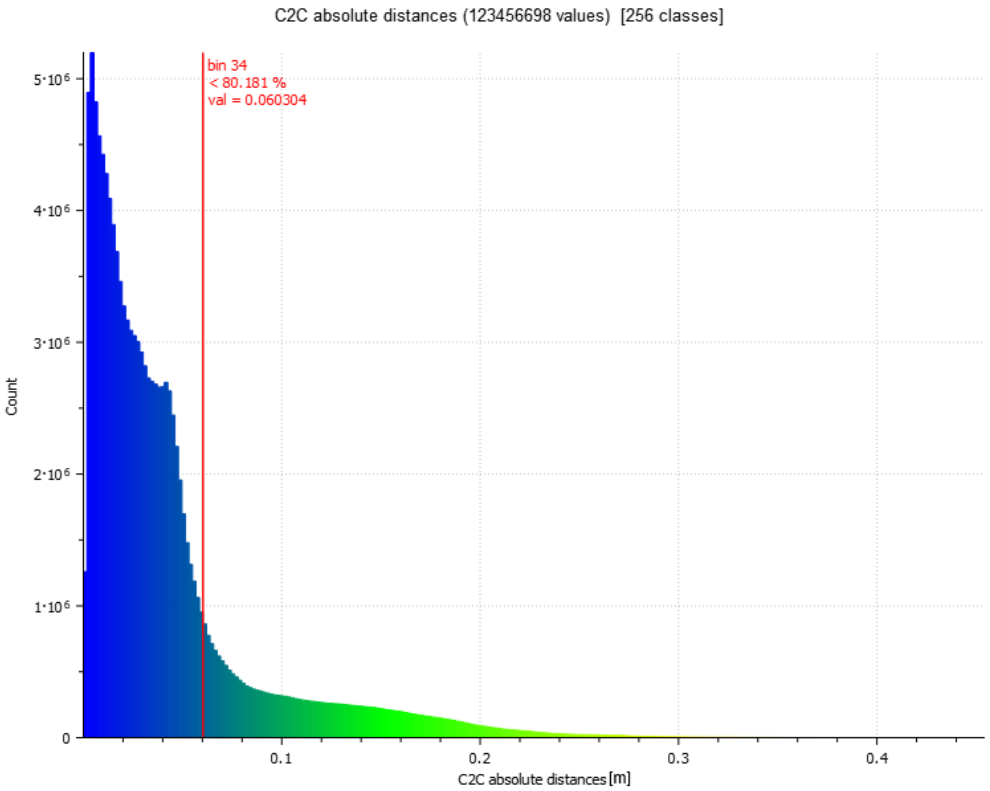

Figure 28. Accuracy validation based on laser scan using C2C absolute distance algorithm of model generated in third trial (rescaled)—histogram.

The validation of the rescaled model also indicates that inspection of a pre-measured section of the mineshaft can provide higher accuracy. In the case of repeatable flights

conducted during the shaft sinking process, the UAV would operate in such an environment, where reference data are already available.

4. Discussion

This article proposes a complementary UAV-based approach to mineshaft inspection. While it does not supplant qualified inspectors, the autonomous collection of photogrammetric information can enhance safety, documentation quality, and situational awareness during the operation and maintenance of the shaft sinking process. Mineshafts and confined spaces more generally pose severe challenges for UAV operation: GNSS denial, ventilation-induced downdrafts, restricted geometry, and sensing interference. Many off-the-shelf platforms cannot reliably perform system and sensor initialization or maintain stable flight under these conditions. Although there has been significant progress in the use of UAVs in underground mines and confined spaces in general [37–43], the application of UAVs for mineshaft inspection without external connection frameworks, theoretically capable of performing autonomous vertical flights exceeding 1 km in both ascent and descent, remains an unexplored research niche. Consequently, the authors developed a dedicated UAV platform, featuring a multi-camera system for photogrammetric measurements, which was a deliberate design choice. The two main advantages of a photogrammetric approach are the rich visual information available for three-dimensional inspection and the significantly lower cost compared to professional LiDAR scanning systems. While the initial flights, performed with only three cameras, demonstrated that the photogrammetric system was promising, the final trials with all six cameras revealed its full potential, both in terms of the quality of visual representation and the geometry of the resulting point clouds.

This paper reports on UAV development from concept to its last performed flight. Although the use of steel line for centering mineshaft lining is not novel for centering during the mineshaft sinking process, using it as a reference and safety constraint for a UAV is a completely new approach and a considered design choice: a roller-guided, non-contact sensing navigation subsystem centering a UAV based on a central vertical as a mechanical restraint. Although the maximal horizontal displacement was greater than anticipated, the authors emphasize that, without the central vertical acting as a mechanical constraint, conducting such a flight safely would not have been feasible.

Repeated test flights conducted in the shaft test structure confirmed the correct operation of the UAV positioning system. During a 20 min flight sessions in a 5 m high steel formwork with a central vertical, the UAV demonstrated reliable and stable behavior. Although the autopilot stabilization algorithms did not maintain perfect centering, no visible pressure on the central vertical was observed. Instead, the UAV slowly drifted around the central vertical in the horizontal plane. The vertical positioning performance was particularly satisfactory, both in hover and during vertical motion with different accelerations.

The underground tests revealed several factors that may have contributed to the unexpected UAV behavior in the shaft. First, strong vertical air movements prevented the barometer from being used for precise altitude estimation. Furthermore, due to the nonlinear relationship between air pressure and altitude, barometric measurements were not sufficiently reliable for estimating vertical displacement over longer flight sections. Second, the surface of the central vertical rope installed in the shaft was heavily contaminated. Despite scraping the rope before the flights, fine dirt particles were visibly detached during operation and formed a cloud near the vertical positioning sensor, which significantly degraded the measurement accuracy. Finally, the force required to deflect the central vertical decreased with increasing height, due to the reduced tension in the steel line at greater distances from its anchor point, was low enough to affect the position estimation process. As the relative position between the UAV and the rope remained almost

unchanged while both the UAV and the deflected rope moved away, by horizontal distance probably exceeding 50 cm from the shaft center, biases began to accumulate in the UAV position estimator. This issue was most likely caused by the higher than expected deflection of the steel line, which significantly reduced its effectiveness as a mechanical constraint in the upper part of the final flight. Nevertheless, the authors consider the proposed approach promising, as alternative solutions, such as roller encoders, may introduce additional mechanical complexity without necessarily improving system robustness under the tested conditions. Therefore, the presented stabilization system will be further developed to improve positioning accuracy and enable the UAV to complete the entire flight without contact with the central guide.

The validation results of the photogrammetric measurements should be interpreted with caution, as the presented flights differed in methodology and were not repeated under identical conditions. Therefore, repeatability could not be quantified, mainly due to the limited access to the GG-1 mineshaft. At the current stage of development, the achieved accuracy of reconstructed 3D models does not allow for reliable quantitative monitoring of the shaft lining condition or small-scale deformations. Moreover, the proposed UAV-based approach should not be regarded as a replacement for geodetic measurements or terrestrial laser scanning in applications requiring millimeter-level accuracy. Nevertheless, the obtained results are sufficient for inspection-oriented tasks, including the identification of potential hazards such as rock fragments, salt encrustations, or structural elements left in the shaft after previous works. Future work will include multiple flights performed according to a consistent methodology to enable a quantitative assessment of measurement repeatability.

Despite the fragility of UAV platforms in comparison with the scale and robustness of mining infrastructure, the authors believe that such systems may become a basic means of mineshaft inspection in the future. The authors' long-term vision is a fully automated UAV-based inspection system incorporating the solutions described in this article. Unfortunately, the development of such a system would require financial resources, technical infrastructure, and personnel involvement beyond the scope of the present research. Nevertheless, the authors intend to continue this work during future shaft sinking projects in Poland.

5. Conclusions

This paper presents a novel approach to mineshaft inspection using a dedicated UAV-based photogrammetric platform. The UAV was developed from the ground up, and the entire design process, from the initial concept to the current operational state, is described in detail. Over four years of surface and underground testing, both the UAV and environmental conditions were evaluated to ensure optimal performance for this application.

The initial underground experiments focused on determining the UAV's maximum possible horizontal displacement under constrained conditions. When pressed against a steel vertical guide, the UAV exhibited a maximum lateral deviation of only 15 cm, confirming the suitability of this guiding concept. The main flight of manually controlled trials with external reference points aimed to capture visual data in a pre-surveyed environment. During a manually controlled flight conducted in highly unfavorable conditions (without the use of a position aiding system), the UAV successfully completed a stable round trip from the bottom of the shaft, capturing over 3000 photographs. The acquired imagery enabled the generation of a well-oriented and accurately scaled photogrammetric 3D model of the shaft, based on external reference. The resulting model was sufficiently detailed to identify the production years of individual tubing segments. For inspection purposes, this level of detail proved entirely adequate. Furthermore, the models spatial accuracy did not deviate

by more than 5 cm when compared with the reference laser scanning model. Complete model-to-model validation was not possible due to insufficient overlap between laser scans. However, considering the general accuracy of control points, significant discrepancies are unlikely.

The final underground experiments, included three flights using a positioning system based on the central vertical mentioned in Section 2.7. Each trial resulted in a different experience.

The first flight, incorporating stabilization system, focused on collecting data from the positioning system. Although the covered distance was approximately 45 m, this trial enabled the reconstruction of a 25 m section of the mineshaft using only an internal reference. This trial was crucial for understanding the principles of photogrammetric measurement without any external reference. The difficulties associated with rapid vertical motion, which ultimately resulted in entanglement in the safety line, were also used as an opportunity to demonstrate the difference in 3D point cloud quality at different vertical velocities.

The second flight, incorporating stabilization system, focused on developing the most effective procedure for collecting photogrammetric data. To achieve this, the returning downward flight was conducted with a yaw offset of 30°. In practice, this approach provided the equivalent of an additional set of six camera viewpoints and significantly improved horizontal image overlap. The point cloud generated from the second trial was therefore considerably better in terms of visual quality, tie point redundancy and surface completeness than the point cloud generated from the first trial. Due to the lack of an internal reference, the point cloud from the second trial was calculated using external manually selected characteristic points rather than dedicated markers. This resulted in accuracy of photogrammetric model of approximately 5 cm compared to the laser scan.

The third and the last trial, incorporating stabilization system, resulted in generating point cloud of approximately 95 m of GG-1 mineshaft. The 3D model was correctly oriented and scaled. Compared with the final documentation of the GG-1 mineshaft, the general height of photogrammetric model differed by only 30 cm. This was achieved using only the internal reference derived from the positioning system readings. Photogrammetric model generated from third flight differed from laser scan for approximately 15 cm. Most of discrepancies occurred in horizontal values which might be addressed to lower image overlap without rotated flight down. Moreover, as mentioned previously, the laser scan used for validation focused primarily on the guide rails rather than on the shaft lining. However the same photogrammetric model but rescaled during alignment differed approximately 6 cm from the laser scan. That indicates flying in a pre-measured environment is beneficial for such inspections. Nevertheless, the UAV developed in this research managed to perform fully stabilized high-altitude flight in confined space. This fact is highly promising for future studies and further development of this system. It should be emphasized that the presented UAV platform is still at the development stage. The difficulties encountered during the current research indicate that further work is required before the system can be considered fully operational and suitable for full-scale autonomous inspections. Real-life underground tests in a mineshaft are particularly challenging due to tight operational schedules, the high costs associated with the shaft sinking process and, in this particular case, the ongoing installation of the final shaft infrastructure. Following removal of the central vertical from the GG-1 mineshaft, our research has concluded for now. Future studies on this matter will be resumed during the next shaft sinking project conducted by Przedsiębiorstwo Budowy Kopalń. Other solutions based on this positioning system will be developed in the SW-4 mineshaft where severe conditions are unsuitable for performing any UAV tests.

Author Contributions: Conceptualization, W.R. and J.S.; methodology, W.R. and J.S.; software, J.S. and A.R.; validation, W.R., J.S. and T.L.; formal analysis, T.L.; writing—original draft preparation, W.R. and J.S.; writing—review and editing, T.L.; supervision, T.L.; project administration, W.R.; funding acquisition, W.R. and J.S. All authors have read and agreed to the published version of the manuscript.

Funding: This research was funded by Polish Ministry of Science and Higher Education (DWD/5/0148/2021 and DWD/5/0292/2021).

Data Availability Statement: The data presented in this study are available from the corresponding author upon reasonable request. Access to the data is subject to approval by Przedsiębiorstwo Budowy Kopalń PeBeKa S.A. due to privacy and safety restrictions related to underground mining infrastructure.

Acknowledgments: The authors would like to thank Przedsiębiorstwo Budowy Kopalń and its mineshaft sinking department KRG Szyby for all the help offered in this project. The authors would also like to thank Przemysław Małek and Jakub Wiśniewski from the PeBeKa mining geodesy department and Marcin Moskal from the O/ZG Rudna mining geodesy department.

Conflicts of Interest: Author Wojciech Rutkowski was employed by the company Przedsiębiorstwo Budowy Kopalń PeBeKa S.A. KGHM Group. The remaining authors declare that the research was conducted in the absence of any commercial or financial relationships that could be construed as a potential conflict of interest.

References

1. Zhao, X.; Deng, L.; Zhou, X.; Zhao, Y.; Guo, Z. A Primary Support Design for Deep Shaft Construction Based on the Mechanism of Advanced Sequential Geopressure Release. *Processes* **2022**, *10*, 1376. [CrossRef]
2. Yi, X.; Ren, L.; Ma, L.; Wei, G.; Yu, W.; Deng, J.; Shu, C. Effects of seasonal air temperature variation on airflow and surrounding rock temperature of mines. *Int. J. Coal Sci. Technol.* **2019**, *6*, 388–398. [CrossRef]
3. Kuang, L.F.; Zhu, Q.Y.; Wang, J.Z.; Wang, B. On a Possible Mechanism of Hydrostatic Pressure on Mineshaft Linings in Western China. *Geofluids* **2022**, *2022*, 4090878. [CrossRef]
4. Małkowski, P.; Kamiński, P.; Neduzha, L. Mobile working platform unit as a mean for improvement of safety and convenience of emergency shaft works. *Min. Mach.* **2021**, *39*, 2–11. [CrossRef]
5. Yang, W.; Marshall, A.M.; Wanatowski, D.; Stace, L.R. An Experimental Evaluation of the Weathering Effects on Mine Shaft Lining Materials. *Adv. Mater. Sci. Eng.* **2017**, *2017*, 4219025. [CrossRef]
6. Nikolaev, P.V.; Tarasov, V.V.; Aptukov, V.N.; Ivanov, O.V. Impact of corrosion of cast iron tubing on residual strength of mine shaft lining. *Gorn. Zhurnal* **2024**. [CrossRef]
7. Government of Poland. Geological and Mining Law Act of 9 June 2011 (Dz.U. 2011 nr 163 poz. 981), 2011. Available online: https://isap.sejm.gov.pl/isap.nsf/DocDetails.xsp?id=WDU20260000069 (accessed on 30 June 2026).
8. Ministry of Energy Poland. Rozporządzenie Ministra Energii z Dnia 23 Listopada 2016 r. w Sprawie Szczegółowych Wymagań Dotyczących Prowadzenia Ruchu Podziemnych Zakładów Górniczych. 2017. Available online: https://isap.sejm.gov.pl/isap.nsf/DocDetails.xsp?id=WDU20170001118 (accessed on 30 June 2026).
9. Shen, Y.; Li, Y.; Li, Z. Application of Intelligent Inspection Robot in Coal Mine Industrial Heritage Landscape: Taking Wangshiwa Coal Mine as an Example. *Front. Neurorobot.* **2022**, *16*, 865146. [CrossRef] [PubMed]
10. Konieczna-Fuławka, M.; Koval, A.; Nikolakopoulos, G.; Fumagalli, M.; Santas Moreu, L.; Vigara-Puche, V.; Müller, J.; Prenner, M. Autonomous Mobile Inspection Robots in Deep Underground Mining—The Current State of the Art and Future Perspectives. *Sensors* **2025**, *25*, 3598. [CrossRef] [PubMed]
11. Dang, T.M.; Nguyen, B.D. Applications of UAVs in Mine Industry: A Scoping Review. *J. Sustain. Min.* **2023**, *22*, 5. [CrossRef]
12. Jarraya, I.; Al-Batati, A.; Kadri, M.B.; Abdelkader, M.; Ammar, A.; Boulila, W.; Koubaa, A. GNSS-Denied Unmanned Aerial Vehicle Navigation: Analyzing Computational Complexity, Sensor Fusion, and Localization Methodologies. *Satell. Navig.* **2025**, *6*, 9. [CrossRef]
13. Chen, J.; Wang, H.; Yang, S. Tightly Coupled LiDAR-Inertial Odometry and Mapping for Underground Environments. *Sensors* **2023**, *23*, 6834. [CrossRef] [PubMed]
14. Akhihiero, D.; Olawoye, U.; Das, S.; Gross, J.N. Cooperative Localization for GNSS-Denied Subterranean Navigation: A UAV–UGV Team Approach. *Navig. J. Inst. Navig.* **2024**, *71*, navi.677. [CrossRef]
15. Polish Geological Institute. Copper and Silver Ores Deposits in Poland. Available online: https://www.pgi.gov.pl/en/mineral-resources/concession-maps.html (accessed on 15 June 2026).
16. Point.laz Web Page. 2026. Available online: https://www.pointlaz.com/solutions/lazaruss (accessed on 15 June 2026).

17. DMT-Group. 2026. Available online: https://www.dmt-group.com/about-us/about-dmt.html (accessed on 15 June 2026).
18. Skala 3D. 2026. Available online: https://skala3d.pl/#oferta (accessed on 15 June 2026).
19. Rutkowski, W. Methods, developments and inspections in mine shaft sinking—A review. *Int. J. Min. Miner. Eng.* **2025**, *16*, 21–60. [CrossRef]
20. PX4 Open Source Autopilot. Available online: https://px4.io/ (accessed on 15 June 2026).
21. Remondino, F.; Fraser, C.S. Digital camera calibration methods: Considerations and comparisons. *Int. Arch. Photogramm. Remote Sens. Spat. Inf. Sci.* **2006**, *36*, 266–272. [CrossRef]
22. Brown, D.C. Close-Range Camera Calibration. *Photogramm. Eng.* **1971**, *37*, 855–866. Available online: http://vigir.missouri.edu/Images/Caltech-Toolbox/papers/Brown71.pdf (accessed on 15 June 2026).
23. Iglhaut, J.; Cabo, C.; Puliti, S.; Piermattei, L.; O'Connor, J.; Rosette, J. Structure from Motion photogrammetry in forestry: A review. *Curr. For. Rep.* **2019**, *5*, 155–168. [CrossRef]
24. Pavlis, T.L.; Serpa, L.F. Accuracy of Structure-from-Motion/Multiview Stereo terrain models: A practical assessment for field geology. *Geosciences* **2023**, *13*, 217. [CrossRef]
25. Berra, E.F.; Peppa, M.V. Advances and challenges of UAV SfM-MVS photogrammetry and remote sensing: Short review. *Int. Arch. Photogramm. Remote Sens. Spat. Inf. Sci.* **2020**, *XLII-3/W12*, 267–272. [CrossRef]
26. Hartley, R.; Zisserman, A. *Multiple View Geometry in Computer Vision*; Cambridge University Press: Cambridge, UK, 2004. [CrossRef]
27. Lin, C.; Zhou, J.; Zhang, W. Linearized Collinearity Equations for Scanned Data. *J. Surv. Eng.* **2020**, *146*, 25–35. [CrossRef]
28. Schindler, K. *Mathematical Foundations of Photogrammetry*; Springer: Berlin/Heidelberg, Germany, 2015; pp. 3087–3103. [CrossRef]
29. Rutkowski, W.; Lipecki, T.; Szczepaniak, J. Cost-Effective Photogrammetric Measurements as Possible Solution for Convergence and Lining Deformations Monitoring in KGHM SW-4 Mineshaft. *IEEE J. Sel. Top. Appl. Earth Obs. Remote Sens.* **2025**, *18*, 24690–24700. [CrossRef]
30. Mendez, A.P.; Whidborne, J.F.; Chen, L. Wind Preview-Based Model Predictive Control of Multi-Rotor UAVs Using LiDAR. *Sensors* **2023**, *23*, 3711. [CrossRef] [PubMed]
31. Agisoft Metashape Professional. 2025. Available online: https://www.agisoft.com/ (accessed on 15 June 2026).
32. James, M.; Robson, S.; d'Oleire Oltmanns, S.; Niethammer, U. Optimising UAV topographic surveys processed with structure-from-motion: Ground control quality, quantity and bundle adjustment. *Geomorphology* **2017**, *280*, 51–66. [CrossRef]
33. CloudCompare. 2025. Available online: https://www.cloudcompare.org/ (accessed on 15 June 2026).
34. CloudCompare M3C2 Plugin. 2025. Available online: https://www.cloudcompare.org/doc/wiki/index.php/M3C2_(plugin) (accessed on 15 June 2026).
35. Nex, F.; Remondino, F. UAV for 3D mapping applications: A review. *Appl. Geomat.* **2014**, *6*, 1–15. [CrossRef]
36. CloudCompare C2C Absolute Distance. 2025. Available online: https://www.cloudcompare.org/doc/wiki/index.php?title=Cloud-to-Cloud_Distance (accessed on 15 June 2026).
37. Dahlquist, N.; Nordström, S.; Stathoulopoulos, N.; Lindqvist, B.; Saradagi, A.; Nikolakopoulos, G. Deployment of an Aerial Multi-agent System for Automated Task Execution in Large-scale Underground Mining. *arXiv* **2025**, arXiv:2501.10262. [CrossRef]
38. Papachristos, C.; Khattak, S.; Mascarich, F.; Alexis, K. Autonomous Navigation and Mapping in Underground Mines Using Aerial Robots. In *Proceedings of the 2019 IEEE Aerospace Conference*; IEEE: Big Sky, MT, USA, 2019; pp. 1–8. [CrossRef]
39. Mansouri, S.S.; Kanellakis, C.; Karvelis, P.; Kominiak, D.; Nikolakopoulos, G. MAV Navigation in Unknown Dark Underground Mines Using Deep Learning. In *2020 European Control Conference (ECC)* ; IEEE: St. Petersburg, Russia 2020; pp. 1943–1948. [CrossRef]
40. Boiteau, A.; Vanegas, F.; Gonzalez, F. Framework for Autonomous UAV Navigation and Target Detection in GNSS-Denied and Visually Degraded Environments. *Remote Sens.* **2024**, *16*, 471. [CrossRef]
41. Chang, Y.; Cheng, L. A Review of UAV Autonomous Navigation in GPS-Denied Environments. *Robot. Auton. Syst.* **2023**, *170*, 104533. [CrossRef]
42. Lin, H.Y.; Zhan, J.R. GNSS-denied UAV indoor navigation with UWB incorporated visual inertial odometry. *Measurement* **2023**, *206*, 112256. [CrossRef]
43. Zhang, R.; Hao, G.; Zhang, K.; Li, Z. Unmanned aerial vehicle navigation in underground structure inspection: A review. *Geol. J.* **2023**, *58*, 2454–2472. [CrossRef]

Disclaimer/Publisher's Note: The statements, opinions and data contained in all publications are solely those of the individual author(s) and contributor(s) and not of MDPI and/or the editor(s). MDPI and/or the editor(s) disclaim responsibility for any injury to people or property resulting from any ideas, methods, instructions or products referred to in the content.